Computers in Biology and Medicine 189 (2025) 109876

Contents lists available at ScienceDirect

Computers in Biology and Medicine

journal homepage: www.elsevier.com/locate/compbiomed

Guiding patient-specific cardiac simulations through data-assimilation of soft tissue kinematics from dynamic CT scan

Martino Andrea Scarpolini [a,b], Giulia Piumini [c], Emanuele Gasparotti [a], Erica Maffei [d], Filippo Cademartiri [e], Simona Celi [a,*], Francesco Viola [f]

[a] BioCardioLab, Bioengineering Unit, Fondazione Toscana G. Monasterio, Massa, Italy
[b] Department of Industrial Engineering, University of Rome "Tor Vergata", Rome, Italy
[c] Physics of Fluids group, University of Twente, Enschede, The Netherlands
[d] SYNLAB SDN, IRCCS, Naples, Italy
[e] Radiology Unit, Fondazione Toscana G. Monasterio, Pisa, Italy
[f] Gran Sasso Science Institute (GSSI), L'Aquila, Italy

ARTICLE INFO

Keywords:
Fluid–structure interaction
Cardiovascular system
Aorta
Patient-specific simulation
Data assimilation
Nudging

ABSTRACT

Fluid–structure interaction (FSI) can be key in the generation of accurate digital replica of cardiovascular systems. To personalize these models, however, several patient-specific parameters need to be measured, which can be challenging to accomplish in a non-invasive manner. Alternatively, the cardiac kinematics of the patient can be extracted from imaging data and then directly imposed as a dynamic boundary condition in the computational model, also incorporating temporal and spatial measurement errors. A more advanced method combines FSI with kinematic driven simulations using data-assimilation. Despite its potential, the application of this technique to complex multi-physics cardiovascular simulations remains limited. In this study, we develop an FSI model of a patient's left ventricle (LV) and aorta, personalized with dynamic imaging data using a Nudging algorithm—a data assimilation technique—which is tailored to each cardiac chamber. In particular, for the LV, which embeds small-scale and irregular endocardial structures (higher measurement errors), the active contraction of the patient is replicated primarily using integral measurements (ventricular volume and surface area). On the other hand, the passive motion of the aorta is guided in the simulation relying directly on the local tissue positions from CT scan. The algorithm's simplicity and zero additional computational cost make it particularly suitable for multi-physics problems. Our results show that the assimilation procedure must be tuned to guide the system toward the measurements within the uncertainty range of the in-vivo data.

1. Introduction

Over the past decade, Fluid–Structure Interaction (FSI) models of the cardiovascular system have gained significant attention [1–8], since they provide an intricate physical representation of the cardiovascular region, thus improving our understanding of its pathologies [4]. Indeed, such computational models allow monitoring of both hemodynamic factors (like blood velocity and pressure) and structural variables (including material point displacements and mechanical stresses) with a higher spatial and temporal resolution with respect to in-vivo scanning techniques. However, exploiting the in-silico models in clinical practice to predict the effects and evolution of pathologies calls for a model calibration on the specific cardiovascular system of the patient. Consequently, as the model complexity grows, the amount of patient information required to calibrate these numerical tools correspondingly increases. More specifically, the personalization of in-silico models requires not only the patient-specific anatomy but also fitting each model parameter using available clinical data. This data can be obtained through various measurement modalities and, clearly, non-invasive techniques must be preferred when dealing with patients in a clinical setting.

In this context, medical imaging represents the most important source of in-vivo information and soft tissue movements can be obtained from 4D imaging techniques like computed tomography (CT), magnetic resonance imaging (MRI), or ultrasound (US) [9]. Hemodynamic quantities can be measured from Phase Contrast MRI or US [10–13]. Recent and ongoing advancements in medical imaging have led to accelerated image acquisition, improved image quality, and minimized patient risk [14–17]. Consequently, dynamic imaging techniques, for

* Corresponding author.
E-mail address: s.celi@ftgm.it (S. Celi).

https://doi.org/10.1016/j.compbiomed.2025.109876
Received 11 July 2024; Received in revised form 30 December 2024; Accepted 4 February 2025
Available online 1 March 2025

example, play now a crucial role in the quantification of motion-related markers, especially in the cardiovascular sector. Additionally, biological materials tend to display very different behavior when characterized in in-vivo, post-mortem, or in-vitro experimentations, making medical imaging even more important [18].

However, these measurements often yield partial observations of the patient's cardiovascular system and the corresponding model's state variables, which are needed to calibrate patient-specific FSI simulations. Firstly, these measurements are either limited to a few locations in space or have limited spatial resolution. Secondly, depending on the specific acquisition modality, different levels of signal-to-noise ratios can substantially impact the quality of the measures. Regarding dynamic modalities, the limited temporal resolution, especially in 4D techniques, often leads to motion artifacts due to patient movement (respiratory cycle, etc.) [19]. Consequently, motion estimation techniques struggle to capture precise tissue motion at small scales [20–22]. Thus, while medical imaging provides critical insights into the patient's condition, the obtained quantities always present uncertainties, are noise-prone, and their non-trivial post-processing might introduce additional errors. This complicates the calibration of the model's parameter and makes it a delicate procedure — and often an ill-posed problem [23,24].

Methodologies for reducing model uncertainties using only partial observations and aligning computational models with experimental/in-vivo observation are employed in many fields of science and engineering and are referred to as Data Assimilation (DA). DA's objective is to take advantage of both model and observations in parallel: on one hand, measurements are used to reduce model uncertainties. On the other hand, the model is used to filter out the observation noise using physical principles and access "hidden" physical quantities not directly measurable by the imaging modality or measurement technique [25].

The possibility to improve the simulation using time-resolved in-vivo data perfectly fits in the framework of data assimilation and has already been explored in several works [10,11,18,20,24,24,26–30]. As reported in Moireau et al. [18], for mechanical models these uncertainties always exist in practice and affect the predictions of the models. Therefore, they should be adequately "filtered" through data assimilation procedures to improve their accuracy. Furthermore, even with perfectly known parameters, filtering the state uncertainties with adequate data always improves the numerical approximation of the system [31].

One key point of data-assimilation approaches is that the instantaneous position of the cardiac tissues obtained from CT is not imposed as a boundary condition as happens in kinematic driven or "Image based CFD" [32–34]. The latter, we recall, uses dynamic imaging data to prescribe arterial (or cardiac) wall displacement, thus avoiding the solution of the structural model and its two-way coupling with hemodynamics. As a consequence, not only the resulting hemodynamics is contaminated by the uncertainties/errors in the patient-data, but the computational domain is constrained to the subset of the cardiovascular system where the patient data is available. Differently, in this study we retain the full FSI modeling of the cardiac anatomy and we include a DA procedure to drive the simulation toward the patient data, where/when available. The advantage is twofold. Firstly, as the patient data are not imposed "stiffly" as a boundary condition, their uncertainty is partially filtered out by the dynamics of the system. Secondly, such approach can cope with the lack of imaging data in a portion of the cardiovascular system, as it allows to exploit patient data where available and to still rely on the FSI modeling where they are not.

The method (based on the Nudging algorithm [25,35,36]) is introduced in Section 2.5 and will be then applied to run an FSI patient-specific simulation guided using dynamic CT Angiography image data acquired over a heartbeat (whose processing is described in Section 2.1). The simulation (whose numerical details are described in Sections 2.2 and 2.4) comprehends a wide portion of the cardiovascular system, including the whole thoracic aorta and the left ventricle. Although CT provides the fine details of the patient's cardiac anatomy (owing to its superior spatial resolution with respect to other scanning techniques), it lacks hemodynamics observables such as blood velocity and pressure. Therefore, we try to fill this gap by leveraging the FSI model, which allows to recover both hemodynamics and mechanical variables when correctly calibrated or driven by patient data.

The key point of our approach lies in the attention devoted to the different signal-to-noise ratios of the measurements of each cardiovascular district (region or cardiac chamber, *i.e.* aorta or left ventricle in our specific setup). The position of material points in time presents a much higher noise in the left ventricle compared to the aortic wall, given its complex multi-scale anatomy and motion. This is addressed by feeding a weighted combination of integral and local measurements into the model, depending on the district.

2. Material and methods

The left ventricle (LV) and thoracic aorta (AO) walls and lumens are considered to model the patient's cardiovascular system. The lumen is described in terms of the blood velocity $\mathbf{u}(\mathbf{x}, t)$ and pressure $p(\mathbf{x}, t)$ in an Eulerian reference system $\mathbf{x}$ and in time t. $\mathbf{y}(t)$ and $\dot{\mathbf{y}}(t)$ represent the Lagrangian position and velocity of the wall's material points, whereas the Lagrangian position measured from CT is indicated by $\hat{\mathbf{y}}(t)$.

2.1. Cardiovascular geometry and kinematics

For this study, we retrospectively analyzed a patient (65 years old, male) not affected by cardiovascular diseases. Patient-specific data is extracted from an ECG-gated dynamic Computed Tomography (CT) Angiography scan, acquired using Siemens, Photon counting Naeotom Alpha CT scanner. Twenty ($N = 20$) image volumes of $512 \times 512 \times 326$ voxels covering the whole thorax ($\mathrm{CT}(t_0)$, …, $\mathrm{CT}(t_{N-1})$) are reconstructed through the cardiac cycle at a heart rate of 91 bpm, resulting in a temporal resolution of $t_{i+1} - t_i = \Delta t = 33$ ms, an in-plane spatial resolution of 0.31×0.31 mm, and a slice thickness of 0.70 mm. Fig. 1a illustrates the clinical dataset showing two different slices of the CT in the end-diastolic configuration (t_0): one in the coronal direction and the other clipping the heart in half (Parasternal Long Axis View (PLAX)). The left and right ventricle (RV), left and right atrium (LA and RA), aorta, and aortic and mitral valves (AV and MV) are visible and highlighted in the two slices. It is evident how the lumen boundaries of the aorta and left ventricle are substantially different (the two green arrows). The aorta has a smoother and more delineated boundary compared to the LV, which contains several smaller structures.

A pre-processing procedure was used to generate a manual segmentation of the aorta and the LV for each cardiac phase acquired with CT scan. Specifically, the 3DSlicer [37] open source software was used for the segmentation while the free software MeshMixer [38] was adopted for a final smoothing and re-meshing process. Fig. 1b illustrates the workflow for extracting patient-specific data from the medical images. The resulting twenty triangular tessellations $s(t_i)$ (purple surfaces in Fig. 1b) represent the aortic and ventricular lumen boundaries at different time points $t_i \in \{t_0, \dots, t_{N-1}\}$ along the cardiac cycle. The first phase t_0 (end-diastolic configuration) is used to create the final tessellation of the in-vivo configuration through a meshing process to obtain a mesh with triangular elements of uniform size (first green surface from left to right in Fig. 1b). The coordinates of the nodes of this mesh will be referred to as $\hat{\mathbf{y}}(t_0)$. A more detailed representation of the structural mesh is reported in Fig. 2, where the in-silico geometry (green) is pinpointed within the whole cardiac geometry of the patient. The other segmentations (see for example $s(t_1)$ and $s(t_{N-1})$ in Fig. 1) are used for *motion estimation* [22], *i.e.*, to measure the movement of each tissue's material point through time. In other words, the other segmentations are used to measure the Lagrangian positions $\hat{\mathbf{y}}(t_i)$ of the material in the deformed configurations $t_1 \dots t_{N-1}$.

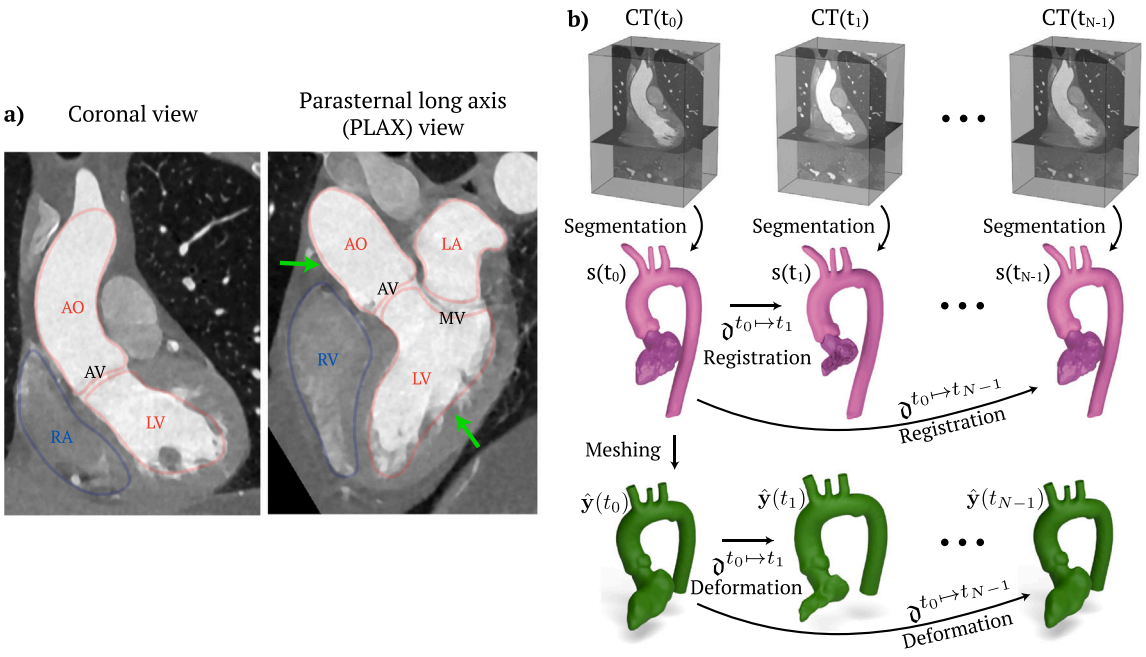

Fig. 1. In-vivo data processing. (**a**): two different slices of the ECG-gated dynamic CT scan in the diastolic configuration (t_0): one in the coronal direction and the other clipping the heart in half (Parasternal Long Axis View). The left and right ventricle (LV and RV), left and right atrium (LA and RA), aorta (AO), and aortic and mitral valves (AV and MV) are visible and highlighted in the two slices. The two green arrows highlight the differences between the aortic and LV lumen boundaries. (**b**): dynamic CT scan image volumes ($CT(t_0), \dots, CT(t_{N-1})$) from which patient-specific information is extracted. A segmentation of the aorta and left ventricle ($s(t_0), \dots, s(t_{N-1})$) is generated from each image volume (purple surfaces). The segmentations $s(t_i)$ are used to estimate the kinematics of the structures by computing a displacement field $\mathfrak{d}^{t_0 \mapsto t_i}$ from t_0 to each t_i. The final tessellation of the in-vivo configurations (green surfaces) is created from $s(t_0)$ through a meshing process, giving $\hat{\mathbf{y}}(t_0)$. Each subsequent configuration $\hat{\mathbf{y}}(t_i)$ is generated applying the ith deformation field $\mathfrak{d}^{t_0 \mapsto t_i}$.

In order to compute the Lagrangian displacements, a surface-based registration process is employed (as opposed to intensity-based registration approaches, which work directly on the imaging data [39,40]). Since the triangular meshes of the segmentation $s(t_i)$ do not have points correspondence through time (*i.e.*, the meshes are not conformal one to each other), a deformation field mapping a reference configuration (say $\mathbf{s}(t_0)$) into the configuration of each other cardiac phase t_i is computed adopting the specific algorithm described in Scarpolini et al. [41]. Briefly, this approach is based on the minimization of a distance function between the reference surface $s(t_0)$ and the target one $s(t_i)$ (Fig. 1b), thus obtaining the displacement fields $\mathfrak{d}^{t_0 \mapsto t_i}$ that map $s(t_0)$ onto $s(t_i)$ for each available time point. In order to apply these deformations onto the final tessellation $\hat{\mathbf{y}}(t_0)$, we interpolate in space each $\mathfrak{d}^{t_0 \mapsto t_i}$ using radial basis functions and obtain the subsequent $\hat{\mathbf{y}}(t_1), \dots, \hat{\mathbf{y}}(t_{N-1})$. In this way, we obtain $N = 20$ tessellations through time $\hat{\mathbf{y}}(t_i)$ with point correspondence. It should be noted that the registration is done between lumen boundaries and not material points. Consequently, the measured displacement vectors will have a higher accuracy on their surface normal component with respect to the tangential ones, which are partially overlooked by the registration procedure, as also explained in Moireau et al. [26]. This phenomenon must be taken into account when analyzing results, as the tangential displacement of myocites connected to the helicoidal motion during systolic contraction, for example, will be partially overlooked by the method.

Furthermore, it is important to notice that these measurements will have different accuracies depending on the structure. As shown in Fig. 1a, the presence of complex small-scale structures on the LV wall (papillary muscles and trabeculae) makes it more difficult to clearly delineate a boundary surface. This difference will be addressed in Section 2.5 by developing an assimilation procedure that takes this lack of knowledge into account.

In addition to Lagrangian positions, integral quantities of every single structure have been measured. In particular, the volume and area of the left ventricle ($\hat{V}_{LV}(t_i)$ and $\hat{A}_{LV}(t_i)$) and aorta ($\hat{V}_{AO}(t_i)$ and $\hat{A}_{AO}(t_i)$) have been measured using the Lagrangian positions $\hat{\mathbf{y}}(t_i)$ at each corresponding cardiac phase t_i. Additional clinically interesting quantities, such as End Diastolic Volume (EDV) and End Systolic Volume (ESV), are measured as well. Measurement errors for these integral quantities have been estimated by computing the inter-observer variability: two experts in the medical field independently segmented the same structure in a single cardiac phase (resulting in different Lagrangian positions and, consequently, integral quantities) and the semi-dispersion of the obtained results was used as error, as typically done in the medical imaging community [42,43]. These quantities, together with the estimated errors, are reported in Table 2 and are in agreement with literature values found in Maffei et al. [44] (both values and errors).

Regarding the aortic and mitral valves, it is clear from Fig. 1a that their segmentation is a challenging problem. Recent works show promising results in obtaining the full 3D valvular geometry from CT scans [45]. However, the limited accuracy of these methods, in addition to the problem of measuring their mechanical properties, produces high uncertainties when dealing with FSI simulations. Consequently, in this study, we opted to simply model the heart valves as flat porous surfaces attached to the surrounding tissues (aortic and mitral annuli), an approach usually referred to as "resistive immersed surfaces". Fig. 2a shows these surfaces as white patches inside the heart. This simplified modeling avoids the specification of the leaflets' geometry and works by prescribing opening and closing timing as observed from the CT. Indeed, even if the detailed leaflet geometry is hard to reconstruct, its opened or closed configuration can be easily observed. For example, in the PLAX view of Fig. 1a, the AV is in fully opened configuration, while the MV is fully closed. The time $\tilde{\tau}$ that the valves require to go from fully opened to fully closed configuration is a characteristic parameter. Since the CT temporal resolution is insufficient to capture this time, $\tilde{\tau}$ was set to 40 ms according to measurements performed on subjects with healthy aortic and mitral valves [46,47]. This value corresponds to the lower bound of the literature range (40–160 ms), which was further supported by imaging data. Dynamic CT scans indicated near-complete valve transition between closed and open states within two consecutive

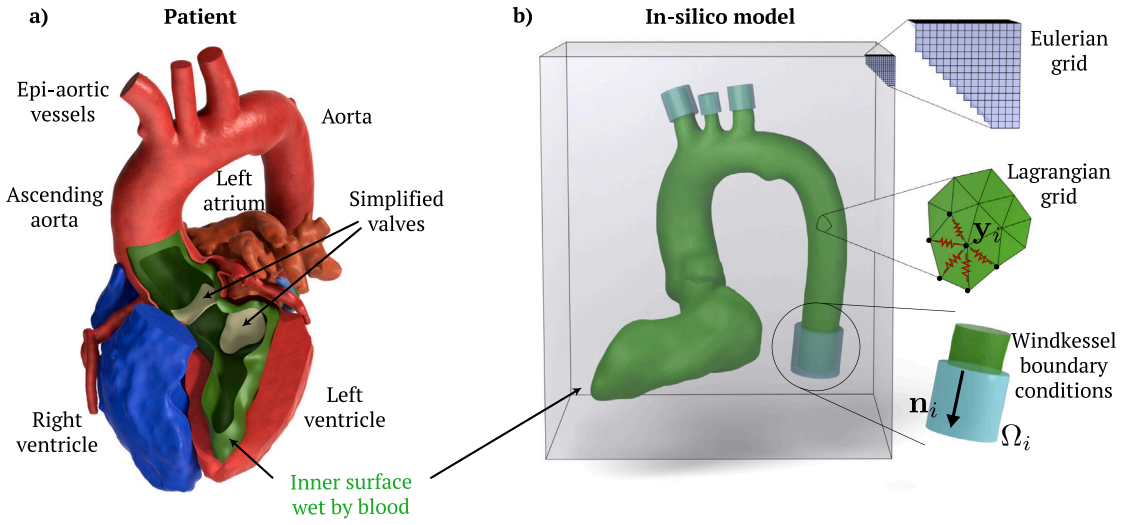

Fig. 2. Comparison between patient-specific complete cardiovascular geometry and in-silico model. Panel (a) shows the complete cardiovascular geometry of the patient, with the right, left ventricle, aorta, coronary arteries and left atrium. The latter is compared in panel (b) to the in-silico model geometry of the left ventricle and aorta (2D surface), depicted in green. These surfaces are discretized with triangular elements (Lagrangian grid) and immersed in the fluid domain, which is discretized as a cartesian mesh (Eulerian grid). At each open artery tip (descending aorta and epi-aortic vessels), the Windkessel model is used to apply appropriate boundary conditions by forcing the fluid in the cyan cylindrical subdomains Ω_i.

acquisitions (approximately 33 ms). In our setup, the effect of opening and closing valves is numerically prescribed by gradually changing the porosity of the valves from zero to infinity.

This simplification is also motivated by the will to keep the focus of the work on the DA procedure rather than complex physical modeling and numerical techniques required to model the valves (see for example [48]).

2.2. Fluid dynamics

The blood velocity $\mathbf{u}(\mathbf{x},t)$ and pressure $p(\mathbf{x},t)$ are governed by the incompressible Navier–Stokes equations:

$$\begin{cases} \rho\left(\partial\mathbf{u}/\partial t + \nabla\cdot(\mathbf{uu})\right) = -\nabla p + \nabla\cdot\boldsymbol{\tau} + \mathbf{f}_{\mathrm{IB}} + \mathbf{f}_{\mathrm{WK}} \\ \nabla\cdot\mathbf{u} = 0 \end{cases} \tag{1}$$

where $\rho = 1060\ \mathrm{Kg/m^3}$ is the constant blood density. The blood is modeled as an incompressible Newtonian fluid, so the viscous stress tensor is given by $\boldsymbol{\tau} = \mu(\nabla + \nabla^T)\mathbf{u}$ with $\mu = 3.5$ mPa s representing the blood viscosity with a hematocrit of 40% [49,50]. Eq. (1) are solved in nondimensional units over a Cartesian mesh using central second-order finite differences discretized on staggered grids [51,52] and are marched in time using a fractional step with an explicit Adams–Bashforth method for the non-linear convective term and an implicit Crank–Nicolson method for the viscous terms. The nondimensionalization process results in a Reynolds Number $Re = \rho U L/\mu = 6133$, where $U = 0.75\ \mathrm{m\,s^{-1}}$ and $L = 27$ mm are the characteristic velocity and length scales used for nondimensiolization. Given the transitional nature of the flow at a Reynolds number of ~ 6000, we perform a Direct Numerical Simulation (DNS) of the Navier–Stokes equations. The cartesian mesh is composed of $n = 366 \times 484 \times 484 \simeq 8.6 \cdot 10^7$ equally spaced grid points, distributed every 370 μm in each direction. The no-slip condition on the moving wet cardiovascular tissues is imposed through the instantaneous forcing $\mathbf{f}_{\mathrm{IB}}$ using an Immersed Boundary Method (IBM) based on the moving least square (MLS) interpolation [53–55]. As it happens in IBMs, the cardiovascular structures (Lagrangian grid) are immersed in the fluid domain (Eulerian grid), as shown in Fig. 2b. The hydrodynamic loads acting on the wet tissues are computed as:

$$\mathbf{f}^H = (-p\mathbf{n} + \boldsymbol{\tau}\cdot\mathbf{n})\,ds \tag{2}$$

being $\mathbf{n}$ the wet normal direction.

As visible in Fig. 2b, the tips of the arteries and the left ventricle representing the inlets/outlets of our cardiovascular domain do not cross the boundaries of the fluid computational domain. During the cardiac dynamics, blood is sucked from the outer volume through the mitral valve opening and propelled towards the same outer volume through the aorta and epi-aortic vessels. To model the impact of the truncated cardiovascular tree and obtain realistic blood pressure in the heart chambers, appropriate lumped parameters models should be used as boundary conditions. For the descending aorta and epi-aortic vessels, we used the Windkessel model which describes the peripheral resistance and arterial compliance by solving the equivalent electrical circuit with two resistances R_d and R_p and a capacitor C. These three parameters are tuned to obtain standard physiological pressure (80–120 mmHg) [56–58] and are reported in Table 1 for each clipped artery. Their calibration is described in the next section.

The pressures provided by the Windkessel model are imposed through the volume forcing $\mathbf{f}_{\mathrm{WK}}$ in Eq. (1), which is only active in the cylindrical subdomains Ω_i (having outward-pointing normal vector n_i, as in Fig. 2b). The forcing is homogeneous inside each subdomain and dynamically computed at each time step using a proportional–integral–derivative (PID) controller on the error value $e_{\Omega_i} = (p_{\Omega_i} - p^{\mathrm{WK}}_{\Omega_i})$, where p_{Ω_i} is the average pressure measured at the inward-facing base of the cylinder Ω_i, and $p^{\mathrm{WK}}_{\Omega_i}$ is the pressure obtained by solving a three elements Windkessel model for that specific subdomain. On the other hand, owing to the lower pressure loads inside the left atrium, on the mitral opening we set a zero pressure condition (which corresponds to sucking blood directly from the outside box when the valve is opened).

2.3. Windkessel calibration

The Windkessel parameters regulate the pressure at each artery tip based on their blood outflow, which in turn depends on the hemodynamic variables on the whole domain and their interaction with the structure deformations. A specific iterative calibration process for the Windkessel parameters calculation was defined by calculating an initial guess and then refining the parameter by using the results of the FSI simulation. The initial guess of the Windkessel parameters is needed to reduce the computational cost of the calibration procedure. To this aim, an estimation for the net flowrate through the four outlets during systole (descending aorta and the three epi-aortic vessels, while the mitral valve is sealed) $q_i(t)$ can be inferred by the increasing/decreasing

Table 1
Windkessel model parameters for each subdomain Ω_i: Descending Aorta (DA), Brachiocephalic Artery (BCA), Left Common Carotid Artery (LCCA) and Left Subclavian Artery (LSA). Distal and proximal resistances R_d and R_p are given in units of $\mathrm{kg\,m^{-4}\,s^{-1}} \times 10^6$ and the capacitance C is given in $\mathrm{m^4\,s^2\,kg^{-1}} \times 10^{-9}$.

Ω_i	R_d	R_p	C
DA	326.3	14.21	3.675
BCA	917.6	38.88	1.293
LCCA	2402.3	61.08	0.437
LSA	1190.2	51.12	1.004

aortic ($V_{AO}(t)$) and ventricular (V_{LV}) volumes measured from in-vivo data. The total blood entering the aorta $q_{\mathrm{tot}}(t)$ is estimated as

$$q_{\mathrm{tot}}(t) = \sum_i q_i(t) = -\frac{d\hat{V}_{LV}}{dt}\bigg|_{\mathrm{systole}} - \frac{d\hat{V}_{AO}}{dt} \tag{3}$$

while the subdivision of $q_{\mathrm{tot}}(t)$ to each outlet can be approximated based on their respective cross-sectional areas A_i, as in Youssefi et al. [59], Boccadifuoco et al. [57]

$$q_i(t) \simeq \frac{q_{\mathrm{tot}}(t) \cdot A_i}{\sum_i A_i} \tag{4}$$

To find the Windkessel parameters in the absence of direct in-vivo pressure measurements, our approach is to replicate physiological conditions. Specifically, this was done by choosing a pressure range between 80 and 120 mmHg at each vascular outlet. This strategy has been adopted in several works in literature [57,60,61] and the calibration process can be conducted either manually or through an automated approach utilizing optimization algorithms. Given the flow rates $q_i(t)$, each iteration of the calibration requires merely the resolution of a set of ordinary differential equations, thus proceeding almost instantaneously. Here, the optimization procedure is carried out through a differential evolution algorithm [62], which utilizes an objective function designed to maintain the obtained pressure profile bounded inside the standard physiological range of 120 and 80 mmHg. A similar approach can be found in Antonuccio et al. [63]. The optimization is subject to an additional constraint on the characteristic time $\tau = R_d \cdot C$, which is confined within the interval of 0.3 to 4 s to ensure physiological relevance. Finally, subsequent FSI simulations are iteratively repeated until the Windkessel parameters reach convergence. This iterative process is necessary for FSI simulation because the flow at outlets ($q_i(t)$) depends on the structure's compliance. In our case, two iterations were sufficient, achieving parameter variation below 1%. The final parameters used in this study are reported in Table 1.

2.4. Structural mechanics

The dynamics of the deformable cardiovascular tissues are solved using a spring-network structural model based on Fedosov's interaction potential approach [64,65]. A mechanical solver for thin shells is used for both the left ventricle and aorta which are discretized as triangulated surfaces. The structural model is built considering the triangulated network of springs (see for example the inset about the Lagrangian grid in Fig. 2), one for each edge. The mass of the structure is concentrated on the vertices of the triangles, uniformly distributed among them. The potential energy of the system accounts for the in-plane and bending stiffness of the tissues. In particular, the out-of-plane deformation of two adjacent triangles sharing an edge is modeled by means of a bending spring, whose elastic constant depends on the continuum elastic properties and the local tissue thickness. A detailed explanation, together with an explicit derivation of the forces acting on the mesh nodes, is given in de Tullio and Pascazio [53].

Several models of the elasticity of the myocardium are available in the literature, also accounting for its orthotropic properties [2,66]. In this work, a simple linear elastic material was used since the major focus was the DA technique and a detailed description of the cardiovascular tissue properties was out of the scope. Moreover, the adoption of a material model able to cope with the fiber architecture introduces a set of unknown and uncertainties that, at the state of the art, are impossible to be derived from in-vivo CT images. The Young elastic modulus of the aortic tissue $E = 0.36$ MPa was chosen so as to reproduce the average one measured from the in-vivo Lagrangian displacements using a recent method from Celi et al. [21], while for the left ventricle $E = 60$ kPa was chosen according to literature ranges [26,67]. The wall thickness is considered uniform in the cardiac chambers and set to $h_{AO} = 2.7$ mm for the aorta and $h_{LV} = 8$ mm for the ventricle following physiological values in Viola et al. [2] and clinical studies [68–70].

The contraction and relaxation of the left ventricle along with the passive motion of the aorta result from the dynamic balance among the inertia of the tissues $m\ddot{\mathbf{y}}$, the external hydrodynamic forces given by the fluid solver $\mathbf{f}^H$ in Eq. (2), the internal passive forces coming from the structural solver $\mathbf{f}^I$ and the "Data Assimilation forces" $\mathbf{f}^N$ generated w.r.t. in-vivo measurements (detailed description in the next section):

$$m_i\ddot{\mathbf{y}}_i = \mathbf{f}_i^I + \mathbf{f}_i^H + \mathbf{f}_i^N \tag{5}$$

where m_i is the concentrated mass of the ith Lagrangian node and $\mathbf{y}_i$ is its position. In the human heart, the active contraction of the myocardium is normally triggered by the activation potential signal [1]. To simulate this, digital heart models must recreate this signal coupling an Electrophysiology (EP) model to the fluid–structure interaction equations [5,71,72]. Instead, in this work, we do not resort to any EP model, and the effect of the active ventricular contraction is naturally incorporated in the "Data Assimilation forces" driven by the CT data (the contribution given by $\mathbf{f}_i^N$), as will be described in Section 2.5. The node index i will be dropped in the following equations to keep the notation simple.

In order to integrate Eqs. (1) and (5), a loose coupling approach is used where the fluid is solved first and the generated hydrodynamic loads are used to evolve the structure, whose updated configuration is the input for the successive time step. This approach is computationally cheaper than a strong coupling approach but is prone to numerical instability, and a small time step (here $dt = 1$ μs) has to be used to ensure numerical stability. Additional details about this choice are discussed in Viola et al. [2], Verzicco [1].

The numerical system resulting from the discretization of the fluid–structure interaction (FSI) problem demands substantial computational resources. To address this, the multiphysics solver used in this work is implemented using CUDA Fortran to harness the benefits of highly parallel multi-GPU computing, eliminating the need for large-scale supercomputing facilities. Further details on the implementation and scalability of this approach can be found in Viola et al. [3]. The proposed assimilation strategy (nudging) adds a negligible computational cost to the simulation, without impacting the time needed to solve the original FSI problem. For this study, each simulation is conducted on a single Nvidia A100 80 GB GPU, with each cardiac cycle requiring approximately 14 h to compute.

The initial conditions of the structural mesh are initialized from the in-vivo model in order to obtain anatomical personalization of the model. However, $\hat{\mathbf{y}}(t_0)$ is associated with the in-vivo end-diastolic configuration (with a typical arterial pressure of 80 mmHg) and thus does not correspond to the stress-free configuration that is needed to initiate the structural solver. Hence, the stress-free configuration has been estimated through a weighted reverse displacement method [73,74], which is detailed in Appendix A.

2.5. Data assimilation procedure

The system of FSI governing Eqs. (1) and (5) and the corresponding initial and boundary condition can be recast in the form of a dynamic

Table 2
Ventricular parameters compared between in-vivo measurements and three in-silico experiments NLV1, NLV2 and NLV3 at different nudging settings. End Diastolic Volume (EDV), End Systolic Volume (ESV), Stroke Volume (SV), Ejection Fraction (EF) and Cardiac Output (CO) are reported. For experiment NLV1 the quantities are not reported since it stops during the systolic contraction due to a collapse of the structure. The discrepancy ($x_{\text{in-silico}} - x_{\text{in-vivo}}$) between in-silico and in-vivo quantities are reported in the last three columns.

Quantity		In-vivo	In-silico			In-vivo/in-silico discrepancy		
			NLV1	NLV2	NLV3	NLV1	NLV2	NLV3
EDV	mL	75 ± 2	–	74.8	73.9	–	−0.2	−1.1
ESV	mL	23 ± 3	–	24.9	25.5	–	1.9	2.5
SV	mL	51 ± 3	–	49.8	48.4	–	−1.2	−2.6
EF	%	69 ± 4	–	66.6	65.5	–	−2.4	−3.5
CO	L min^{-1}	4.7 ± 0.3	–	4.5	4.4	–	−0.2	−0.3

system as follows:

$$\begin{cases} \dot{\mathbf{X}} = \mathcal{M}(\mathbf{X}, t) \\ \mathbf{X}(t_0) = \mathbf{X}_0 \end{cases} \tag{6}$$

where $\mathbf{X}$ is the state vector, *i.e.*, the collection of variables describing our system and are evolved by the model. In this work the state vector is composed by both structural and hemodynamics variables, *i.e.*, $\mathbf{u}(\mathbf{x}, t)$, $p(\mathbf{x}, t)$, $\mathbf{y}$ and $\dot{\mathbf{y}}$, while the dynamical model $\mathcal{M}$ are the fluid and structural Equations ((1) and (5), respectively), as described in 2.2 and 2.4. $\mathbf{X}_0$ is the initial conditions vector. The general principle of DA consists of using some available measurements $\mathbf{Z}$ to improve the predictions of the computational model [25,36,75]. There are two main categories of DA algorithms: sequential, like the one used in this work, and variational. Variational approaches guide the model by minimizing a suitable cost function involving the difference between the data and the corresponding outputs from the simulation. Sequential algorithms directly incorporate the observations $\mathbf{Z}$ into the system by modifying the dynamical model (6). This is done by defining the gain $\mathcal{G}$ and observation $\mathcal{H}$ operators and redefining Eq. (6) into

$$\begin{cases} \dot{\mathbf{X}} = \mathcal{M}(\mathbf{X}, t) + \mathcal{G}[\mathbf{Z} - \mathcal{H}[\mathbf{X}, t]] \\ \mathbf{X}(t_0) = \mathbf{X}_0 \end{cases} \tag{7}$$

where $\mathcal{H}$ models the measurement process on the system by extracting the measures from the state vector [35,76]. For example, $\mathcal{H}(\mathbf{X}, t)$ could represent the measurement of the volume $V(t)$ of a certain anatomical structure from the coordinates of its material points $\mathbf{y}(t)$. If $\mathbf{X}$ was the exact system state, then the observations $\mathbf{Z}$ would be $\mathbf{Z} = \mathcal{H}(\mathbf{X}, t) + \xi$, where ξ is the noise related to the measurement process. The operator $\mathcal{G}$ acts as a sort of inverse of $\mathcal{H}$, transforming the discrepancy between the measured quantity $\mathbf{Z}$ and the analogous model's prediction $\mathcal{H}(\mathbf{X}, t)$ into a correction for the state $\mathbf{X}$. In other words, Eq. (7) nudges the state vector $\mathbf{X}$ towards the observations $\mathbf{Z}$ by adding a forcing that is proportional to their discrepancy $\mathbf{Z} - \mathcal{H}(\mathbf{X}, t)$.

Classical sequential DA like the Kalman filter [25,77], however, are intractable when the model $\mathcal{M}$ contains non-linear partial differential equations (as in our case) and the state vector belongs to a high dimensional space [10,25,26]. This is because they require the computation of covariance matrices, which have the size of the state vector. Consequently, "simplified" versions of sequential DA algorithms have been developed when dealing with complex systems. From one side, reduced order Kalman filters can be developed by constraining the uncertainties to smaller spaces, for example, as in Moireau and Chapelle [78]. Another approach is to use simpler filtering methods that do not consider the uncertainties distributions and stem from control theory, for example the popular Nudging technique [25,35,36,79], otherwise known as Luenberger observer in control theory [26]. Our specific approach resembles the latter and involves the introduction of potentials that penalize the departure of the system from the measurements. Specifically, as discussed in 2.1, our observations of the system $\mathbf{Z}$ include integral quantities like the volume V and area A of anatomical structures, and the local positions $\hat{\mathbf{y}}(t)$ of these structures. Consequently, we introduced the potentials defined in Spandan et al. [54]:

$$\begin{cases} W_V = \frac{1}{2} k_V \left(\frac{V - \hat{V}}{\hat{V}} \right)^2 \hat{V} & \text{(Volume)} \\ W_A = \frac{1}{2} k_A \left(\frac{A - \hat{A}}{\hat{A}} \right)^2 \hat{A} & \text{(Area)} \\ W_P = \frac{1}{2} k_P (\mathbf{y} - \hat{\mathbf{y}})^2 & \text{(Lagrangian Position)} \end{cases} \tag{8}$$

Applying the minimum energy concept, we obtain the "nudging" force $\mathbf{f}^N$ in Eq. (5) by differentiating the potentials with respect to displacements:

$$\mathbf{f}^N = -\frac{\partial}{\partial \mathbf{y}} \left(W_V + W_A + W_P \right) \tag{9}$$

It can be shown that this approach is a variation of the Nudging technique, which is a particular case of Eq. (7), where the gain operator $\mathcal{G}$ does not take into account covariance matrices [35], *i.e.*, it reduces to a multiplicative factor weighting the discrepancy between the simulation and the in-vivo observation. In fact, if we break up $\mathbf{f}^N$ into each one of its components $\mathbf{f}^N = \mathbf{f}^{N(V)} + \mathbf{f}^{N(A)} + \mathbf{f}^{N(P)}$ (volume, area and positions) and we manipulate Eq. (9), we obtain

$$\begin{cases} \mathbf{f}^{N(V)} = -k_V \frac{1}{\hat{V}} \frac{\partial V}{\partial \mathbf{y}} (V - \hat{V}) \\ \mathbf{f}^{N(A)} = -k_A \frac{1}{\hat{A}} \frac{\partial A}{\partial \mathbf{y}} (A - \hat{A}) \\ \mathbf{f}^{N(P)} = -k_P (\mathbf{y} - \hat{\mathbf{y}}) \end{cases} \tag{10}$$

This last equation highlights the proportionality of the forcing terms $\mathbf{f}^N$ to the discrepancy between the predicted and measured quantities ($V - \hat{V}$ for example). The two derivatives $\partial V/\partial \mathbf{y}$ and $\partial A/\partial \mathbf{y}$ can be computed by expressing both volume and area in terms of surface integrals and then by discretizing them on the triangulated surfaces (see [80] for a detailed derivation), while k_V, k_A and k_P are the nudging constants (or "gaining parameters") that must be calibrated. Appendix B illustrates how these constants can be roughly estimated from the physical parameters of the system. Being the forcing terms completely explicit, the nudging procedure does not increase the computational cost of the simulation.

Since our observations have different amounts of noise depending on the specific structure, we define different nudging constants for each of them. In fact, as can be observed in Fig. 1a where both the aorta (AO) and left ventricle (LV) are visible, the aortic lumen has a far smoother and more regular boundary compared to the ventricular endocardium (highlighted by the two green arrows). On the other hand, the ventricular walls are characterized by several multi-scale irregularities that are not present in the aortic ones (*e.g.*, papillary muscles and trabeculae). This makes the segmentation process of the aortic lumen easier and less prone to errors. Consequently, measurements of the aortic wall motion $\hat{\mathbf{y}}(t)$ are accurate enough to be used for guiding the FSI simulation without resorting to an additional nudging on integral geometric quantities (*e.g.*, area and/or volume). In contrast, the latter are necessary for guiding the ventricular dynamics, owing to the higher noise in the local measuring the ventricular endocardium. Consequently, in Section 3 the active LV contraction (Section 3.1) and the passive aortic motion (Section 3.2) will be analyzed separately.

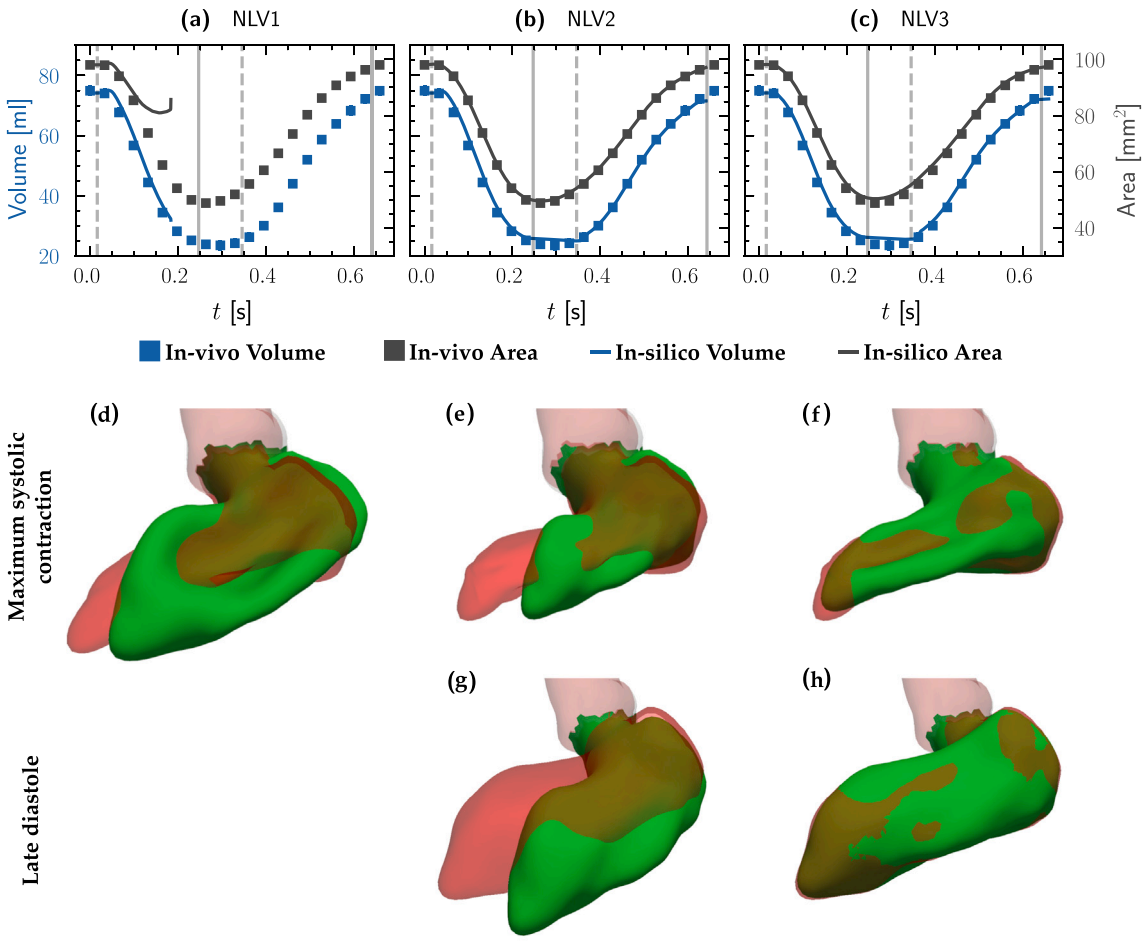

Fig. 3. Comparison between in-silico and in-vivo ventricular contraction at different nudging settings (Experiments NLV1, NLV2 and NLV3). Experiment NLV1 (panels a,d)): nudging only the LV volume ($k_V = 10$, $k_A = 0$, $k_P = 0$); Experiment NLV2 (panels b,e,g)): nudging the LV volume and surface area ($k_V = 10$, $k_A = 1000$, $k_P = 0$); Experiment NLV3 (panels c,f,h)): nudging volume, area and Lagrangian positions of LV ($k_V = 10$, $k_A = 1000$, $k_P = 10$). For each experiment, the LV volume V_{LV} and LV surface area A_{LV} are reported, together with in-vivo measurements. The gray vertical lines in panels (a-c) represent the opening (dashed lines) and closing (solid lines) times of the aortic and mitral valves imposed, as discussed in Section 2.4. Moreover, the in-vivo (transparent red) and in-silico (transparent green) LV configurations are shown for each experiment at maximum systolic contraction (panels d-f) and late diastole (panels g,h). The interrupted solid lines in panel (a) indicate that it was not possible to integrate an entire heart beat and, consequently, the corresponding diastolic snapshot is not reported.

3. Results

3.1. Nudging the ventricular contraction

As explained in Section 2.4, we do not use any EP model in this study to solve the active tension of the ventricular myocardium. Instead, the ventricular contraction observed from the dynamic CT scan is reproduced using only DA, which, in this sense, replaces EP. Hence, nudging forces are crucial in the left ventricle dynamics, as they drive the simulation by generating the active contraction. In the aorta, on the other hand, these forces will act more as a "correction" term of the dynamics, as explained in the next section.

The active LV contraction reproduced with different nudging settings is analyzed for integral quantities only and successively employing the punctual information on the local endocardium position. Each setting is compared with all the available in-vivo measurements. Three different simulations are performed: experiments NLV1, NLV2 and NLV3. Firstly, experiment NLV1 uses only volume nudging with $k_V = 10$ and $k_A = k_P = 0$, while experiment NLV2 adds surface area information, with $k_V = 10$, $k_A = 1000$ and $k_P = 0$. Lastly, experiment NLV3 also relies on the instantaneous position of the endocardium markers, with $k_V = 10$, $k_A = 1000$ and $k_P = 10$. For all three experiments, nudging on the aorta is set to a minimum non-zero value in order to regularize its motion ($k_V = k_A = 0$ and $k_P = 0.1$).

End Diastolic Volume (EDV), End Systolic Volume (ESV), Stroke Volume (SV), Ejection Fraction (EF), and Cardiac Output (CO) are the main clinical functional parameters of the ventricle that can be directly measured from in-vivo data and can be used to validate the DA procedure. Table 2 reports these quantities for the in-vivo measurements and the three experiments, respectively. While NLV2 and NLV3 reproduce each functional parameter inside the measurement uncertainty, NLV1 experiment stops during the systolic contraction due to elastic instabilities. Volume nudging ($\mathbf{f}^{N(V)}$) tends to decrease the volume of the ventricle, while the structural model contrasts it by keeping the myocardium strain as low as possible, leading to a collapse of the structure, which hinders the numerical solution of the equations. To solve this problem and induce a contraction of the myocardium, we add surface area nudging $\mathbf{f}^{N(A)}$ in experiment NLV2 and NLV3.

Fig. 3a–c shows the LV volume and surface area over time for the three simulations, compared with the in-vivo measurements. Additionally, the LV dynamics is visually represented in Fig. 3d–h overlapping the in-silico (*i.e.*, $\mathbf{y}$ in green) and in-vivo (*i.e.*, $\hat{\mathbf{y}}$ in red) LV surfaces during the maximum volume contraction time instant (end-systolic phase when possible) and during maximum volume expansion (late diastole). Panel (a) shows that in NLV1 the volume follows the in-vivo profile while the surface area remains at higher values, thus preventing the integration of a whole heartbeat in the NLV1 case.

As indicated in both Table 2 and Fig. 3b, experiment NLV2 reproduces faithfully the in-vivo contraction in terms of integral quantities.

This is already an interesting achievement since we are reproducing ventricular functional parameters using only integral measurements that are routinely obtained through non-invasive clinical imaging such as echo-cardiography [81–83]. However, a graphical inspection of Fig. 3e reveals that the precise kinematic is not well reproduced in experiment NLV2. In particular, the LV longitudinal axis is not aligned with the one observed in the in-vivo data. In the real setting, the physiological LV contraction arises from a complex physical system involving the material properties (myocardium fibers orientation [6,84]), the spatiotemporal propagation of the active potential signal, and the visco-elastic surrounding tissues effects. All this missing complexity makes it necessary to nudge additional quantities to reproduce the ventricular deformation with high accuracy. If local measurements, such as the motion of each material point, are available, this information can be used to "guide" the simulation even further. Experiment NLV3 adds point-wise nudging $\mathbf{f}^{N(P)}$ and is able to reproduce the integral quantities (with a slight increase in discrepancy from the measurement values, as shown in the last three columns of Table 2) and the kinematics (Fig. 3)c,f).

The resulting ventricular contraction produces a net flowrate inside the aorta that will be investigated in the next section.

3.2. Nudging the passive aortic deformation

As explained in Section 2.5, the segmentation of the aortic region is less prone to errors owing to its smoother wet surface and better visibility in CT measurements with respect to the LV endocardium. Consequently, Lagrangian positions $\hat{\mathbf{y}}_i(t)$ are more accurate for the aortic lumen. Considering this, the nudging algorithm for the aorta directly employs the Lagrangian positions ($k_P \neq 0$ and thus $\mathbf{f}^{N(P)} \neq 0$) and avoids volume and area nudging ($k_V = k_A = 0$).

The effects of nudging the aorta with different intensities are performed through four experiments: NA1, NA2, NA3, and NA4 with $k_P = 0.1$, $k_P = 1$, $k_P = 10$ and $k_P = 100$, respectively. For each nudging configuration, the assimilation settings for the ventricle will be fixed to experiment NLV3 of the previous section (*i.e.*, $k_V = 10$, $k_A = 1000$ and $k_P = 10$ for the LV). The aim is to find the optimal intensity capable of "relaxing" the simulation towards the in-vivo configuration without forcing measurement errors into the simulation and making the system too numerically stiff. In order to quantify the effects, we can inspect the distance between the in-silico and in-vivo configurations, both locally

$$d_\perp(\mathbf{y},t) = (\mathbf{y}(t) - \hat{\mathbf{y}}(t)) \cdot \hat{\mathbf{n}} \tag{11}$$

and averaging over the whole aorta

$$\overline{d_\perp}(t) = \frac{1}{\hat{A}_{AO}} \int_{\partial\Omega_{AO}} d_\perp(\mathbf{y},t)\, d\Sigma \tag{12}$$

where $\partial\Omega_{AO}$ is the aortic lumen boundary, $\hat{\mathbf{n}}$ is the in-vivo, outward facing normal to the lumen boundary, and $d\Sigma$ is the area of a surface element. We recall that the distance $d_\perp(\mathbf{y},t)$ only accounts here for the normal displacement to the aortic walls, as CT data cannot infer the tangential components.

Fig. 4 compares the different nudging strategies against the available in-vivo data—which is taken as ground truth here—in terms of structural quantities. Each quantity is averaged over two cardiac cycles after periodic stationarity is reached. Fig. 4a compares the aortic volume V_{AO} and $\hat{V}_{AO}$ over time. The measurement error of $\hat{V}_{AO}$ is highlighted through the gray shadow. We observe that the overall volume change of the aorta $V_{AO}^{\max} - V_{AO}^{\min}$ is well reproduced in all four experiments. However, the precise time evolution of V_{AO} is slightly helped by the DA procedure that enables to follow the precise time evolution of the measured data even more accurately, as for the NA3 and NA4 experiments. It can be observed that the case of lower nudging intensity (NA1 and NA2) yields a slightly delayed volume profile with respect to in-vivo measurements, *i.e.*, a smaller volume during the systolic acceleration and a larger one after the systolic peak till the end of the cardiac cycle.

Fig. 4b shows the average normal distance $\overline{d_\perp}(t)$ of Eq. (12) computed between the in-silico and in-vivo aortic walls. The gray shadow around $\overline{d_\perp} = 0$ represents an uncertainty interval estimated as the inter-observer segmentation variability. Specifically, the interval width of $\pm\sigma = \pm 0.11$ mm is computed as the standard deviation σ of the per-vertex normal distance distribution measured between two different segmentations performed by different experts. In Fig. 4b, it can be observed that $\overline{d_\perp}(t)$ is about zero for $k_P = 100$ (strongest nudging setup NA4), but is already quite small for $k_P = 0.1$, *i.e.* in the "lightest" nudging setup NA1. Indeed, in NA1, the maximum value in time of $\overline{d_\perp}(t)$ is around 0.3 mm, which is the resolution of the CT. NA3 and NA4 are the only two setups that are completely inside the uncertainty range, while NA2 shows greater differences, particularly after systole at $t \simeq 0.25$ s.

To inspect the distance between in-silico and in-vivo data more locally, Fig. 4c,e,f,g shows $d_\perp(\mathbf{y},t)$ of Eq. (11) in four cross sections $\pi_1, \pi_2, \pi_3, \pi_4$ along the aorta at $t/T = 0.16$. The material points $\mathbf{y}$ intersected by each plane are shown in polar coordinates by setting the origin at each cross section's median point and the 0° azimuthal angle in the direction defined by the white arrows along the centerline in panel (d). π_1 plane is located at the aortic sinus, π_2 at the ascending aorta, while π_3 and π_4 at the descending section.

The local distance in Fig. 4c,e,f,g shows a similar behavior to the average distance in panel (b). The only two experiments that fall inside the uncertainty range of in-vivo data are NA3 and NA4. NA4 shows a practically zero distance at each azimuthal angle, while NA3 peaks at values of $d_\perp(\mathbf{y},t) \sim 0.11$ mm in the π_1 plane (reaching the boundary of the uncertainty range). Indeed, the aortic sinus is the aortic region with the largest movement, and the greatest differences with respect to in-vivo data are captured here. For NA1 $d_\perp(\mathbf{y},t)$ is maximized in the same region π_1 but reaches values of ~ 1.2 mm.

From Fig. 4, it is clear that the right nudging intensity k_P should be chosen such that the system remains inside the in-vivo measurements uncertainty range. This is satisfied by both experiments NA3 and NA4. To ensure the most accurate alignment with in-vivo data, one might be tempted to always set the nudging intensities to their highest possible values. However, this approach would not be optimal due to the inherent uncertainties in in-vivo measurements. Forcing the simulation to precisely match the in-vivo quantities through high nudging parameters, on one hand, tends to a kinematic-driven simulation, thus inheriting the uncertainties on the reference patient data, and on the other, it results in a numerically stiff system. This picture is further explored by analyzing the hemodynamic quantities.

Fig. 5a,b shows the blood flowrate measured in two different aortic cross sections: at the descending aorta q_{DESC} and at the left subclavian artery (LSA) q_{SA3}. It can be observed that the overall behavior of these quantities is quite similar in all four settings. However, for $k_P = 10$ and $k_P = 100$ (NA3 and NA4), high-frequency oscillations can be observed in the flowrates right after the aortic valve opens (the gray dotted vertical line at $t \simeq 20$ ms). Another footprint of these oscillations is evident in Fig. 4a,b at the corresponding time points. These effects are clearly amplified in a stiff system, such as NA4. At high k_P values, the system tends to become kinematic-driven. When the kinematics imposed is not perfectly compatible—potentially due to measurement errors—the fluid is subjected to abrupt decelerations and accelerations to satisfy the principle of mass continuity. Conversely, employing a weaker nudging strategy allows the natural elasticity of cardiovascular structures to mitigate such rapid changes in the fluid dynamics (capacitive effect). Therefore, a compromise must be reached between a fully coupled fluid–structure interaction (FSI) simulation and a kinematic-driven one, taking into account the uncertainties in each in-vivo measurement and the complexity of the physical model used for the simulation. Consequently, NA3 represents the best setting (among the numerical experiments performed NA1-NA4) that allows an accurate match with in-vivo data through the lightest possible nudging

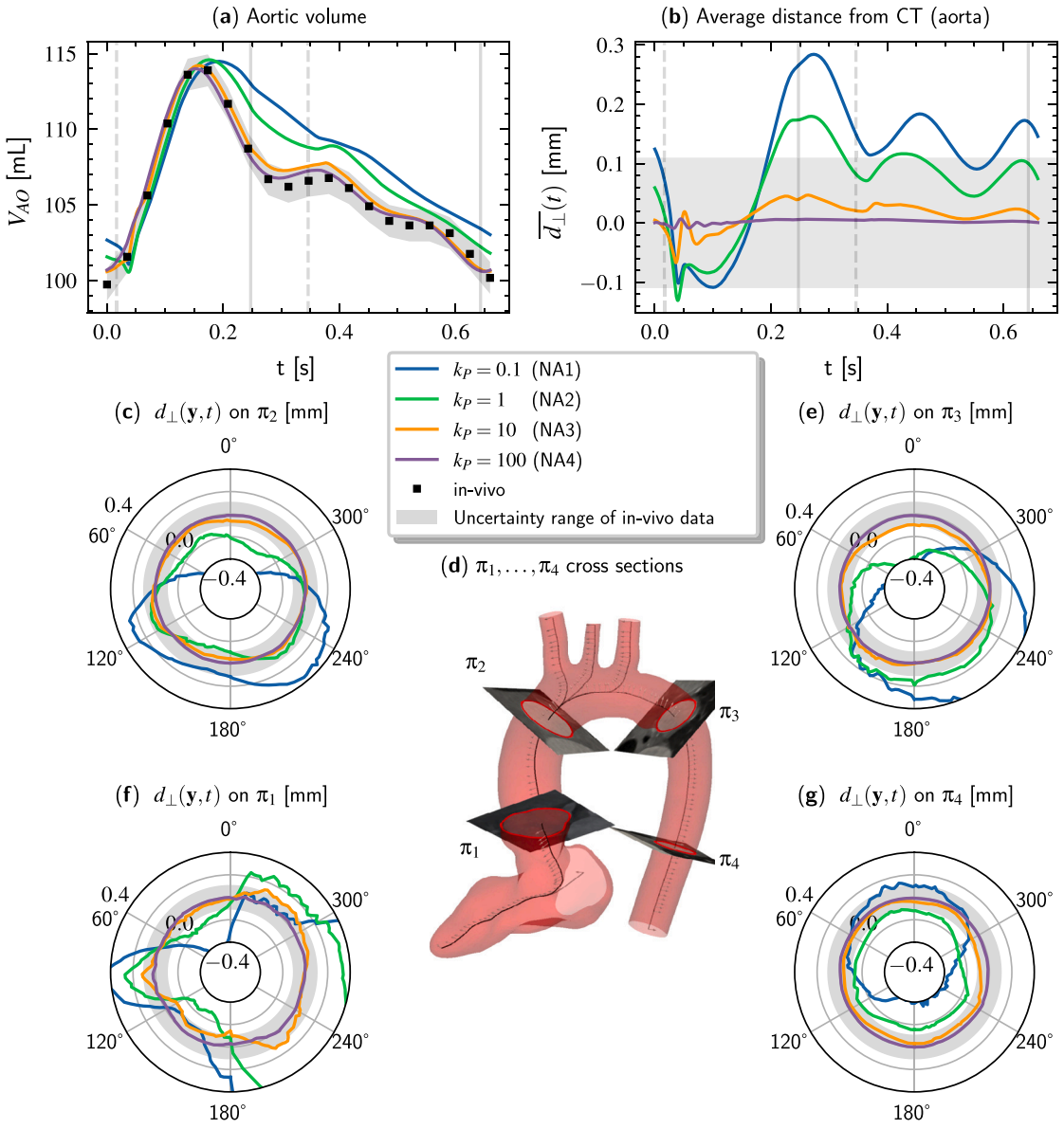

Fig. 4. Comparison of structural results at increasing nudging intensities on the aorta, compared with in-vivo data. Experiments NA1 ($k_P = 0.1$, blue lines), NA2 ($k_P = 1$, green lines), NA3 ($k_P = 10$, orange lines) and NA4 ($k_P = 100$, purple lines) are reported in each plot. Panel (**a**): aortic volume, compared with in-vivo measurements $\hat{V}_{AO}(t)$ (black markers). Panel (**b**): signed distance with respect to in-vivo configuration, averaged over the aortic wall $\overline{d_\perp}(t)$ (Eq. (12)). Panels (**c**,**e**,**f**,**g**) report the same quantity, but locally (Eq. (11)) in specific cross sections $\mathbf{y} \in \pi_1,\dots,\pi_4$, which are shown in panel (**d**). For each cross-section, $\mathbf{y}$ is represented in a polar coordinate system centered at the median point, and the azimuthal angle origin is set in the direction shown in panel (**d**). The gray shadow in the panels represents the segmentation uncertainty, corresponding to the semi-dispersion of two different segmentations, as detailed in Section 2.1.

intensity, thus reducing the stiffness of the system and its oscillations.

In this context, nudging algorithms allow selecting an intermediate setting where the patient's data is introduced into the simulation more gradually rather than being directly imposed. The specific nudging intensity must be carefully chosen (as previously reported in Section 2.5 and other works [85]) to strike a balance between matching the in-vivo observations and limiting the increased stiffness of the resulting system [26].

Further inspection of Fig. 5a,b reveals that for $k_P = 10$ and $k_P = 100$ (NA3 and NA4, respectively), the different $V_{AO}(t)$ profile enhances of 5−10% the flowrate during late systole with respect to NA1 and NA2; 20 mL/s for the descending aorta and 5 mL/s for the LSA. From the inset of Fig. 5a, we also notice that the volume oscillations during the diastolic phase (clearly visible from the in-vivo measurements in Fig. 4a) induce small waves in the descending aorta flowrate, which are not captured in NA1 and NA2.

3.3. Analysis of hemodynamics in a fixed assimilation setting

This section shows the clinically relevant quantities that can be estimated using the nudged-FSI model. Notably, some of them as the blood velocity, the pressure at specific points inside the cardiovascular system, or the hydrodynamical shear stress at the aortic wall, cannot be measured from dynamic CT scans alone. The nudging coefficients for the LV and aorta are fixed to values based on the analysis presented in Sections 3.1 and 3.2. We use experiment NLV3 for LV coefficients, *i.e.*, the one in which both LV functional parameters and the contraction kinematics are correctly reproduced. For the aortic region, the setting of experiment NA3 is used, *i.e.*, $k_P = 10.0$, as a compromise between reproducing the measured Lagrangian positions $\hat{\mathbf{y}}(t_i)$ exactly and avoiding spurious oscillations in the state variables (as shown in Fig. 4a–d).

Fig. 6a shows the ventricular and aortic volumes, compared between in-silico and in-vivo quantities. A good agreement with the latter

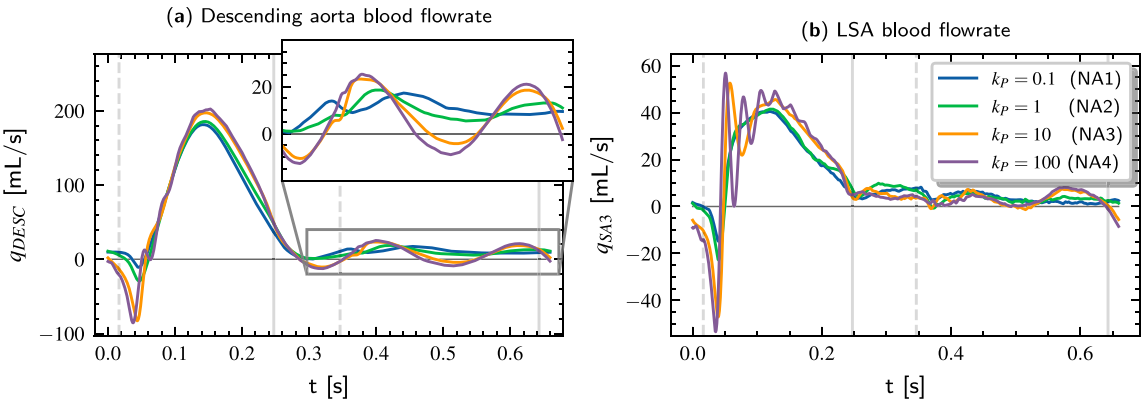

Fig. 5. Comparison of hemodynamic results at increasing nudging intensities on the aorta. Experiments NA1 ($k_P = 0.1$, blue lines), NA2 ($k_P = 1$, green lines), NA3 ($k_P = 10$, orange lines) and NA4 ($k_P = 100$, purple lines) are reported in each plot. Panel (**a**) shows the blood flowrate measured at the descending aorta q_{DESC}, while panel (**b**) shows the blood flowrate measured at the Left Subclavian Artery (LSA) q_{SA3}. Each plotted quantity is averaged over two cardiac cycles after a stationary regime is reached.

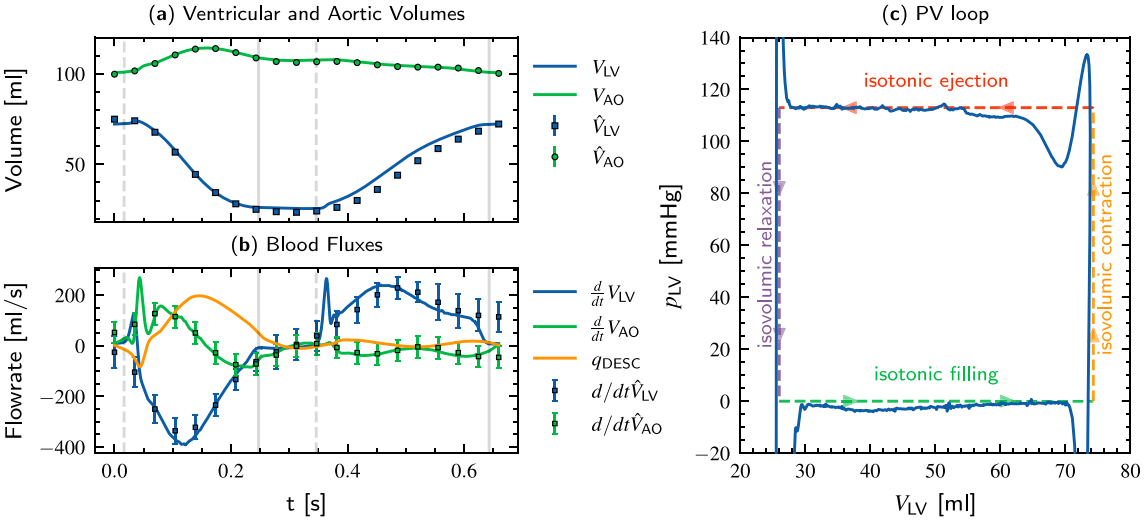

Fig. 6. Model results in a specific Nudging settings. Panel (**a**) shows the ventricular and aortic volumes over time for both the in-silico and in-vivo quantities (V_{LV}, V_{AO} and $\hat{V}_{LV}$, $\hat{V}_{AO}$, respectively). Panel (**b**) shows blood flowrates: time derivatives of ventricular d/dtV_{LV} and aortic d/dtV_{AO} volumes (compared with in-vivo measurements $d/dt\hat{V}_{LV}$ and $d/dt\hat{V}_{AO}$) and flowrates at the descending aorta q_{DESC}. Panel (**c**) shows the PV-loop, *i.e.* the left ventricular pressure p_{LV} plotted versus the volume V_{LV}. Each quantity is averaged over two cardiac cycles after a stationary regime has been reached. The gray vertical lines represent the opening (dashed lines) and closing (solid lines) times of the aortic and mitral valves imposed, as discussed in Section 2.4.

is evident, as already explored in the previous sections. It is clear how the ventricular systole (the region between the first dashed and solid vertical lines) is characterized by a decrease of the ventricular volume V_{LV} that produces a simultaneous increase of the aortic volume V_{AO} caused by the hydrodynamic loads. When the aortic valve closes (first vertical solid line), V_{LV} presents a plateau of around 0.1 s, while V_{AO} has already started its slow relaxation that propels the blood in the diastolic phase. This relaxation lasts till the end of the cycle, while the ventricle is filled up after the mitral valve opening (second dashed vertical line from left).

Fig. 6b shows blood flowrates. Specifically, the time derivatives of the ventricular and aortic volumes are shown and compared between in-silico and in-vivo quantities. dV_{LV}/dt indicates the total blood entering or exiting from the ventricle (compared with $d\hat{V}_{LV}/dt$). dV_{AO}/dt quantifies the aortic compliance (compared with $d\hat{V}_{AO}/dt$). Still in Fig. 4b, q_{DESC} is the flowrate at the descending aorta outlet. The errors of the measured quantities (vertical bars in Fig. 4b) are computed by propagating the initial errors ΔX (ΔV_{LV} and ΔV_{AO} estimated following Section 2.1) to time-derivatives using $\Delta(dX/dt) = \sqrt{2}\Delta X/\Delta T$ following standard error propagation methods [86]. Given the low time resolution of the in-vivo data, we can observe that the error of $d\hat{V}_{LV}/dt$ and $d\hat{V}_{AO}/dt$ increases substantially with respect to $\hat{V}_{LV}$ and $\hat{V}_{AO}$ (which are too small to be visible). It is interesting to notice how the aortic compliance is quite high, storing around 29% of the stroke volume $|V_{\text{AO}}^{\max} - V_{\text{AO}}^{\min}| \simeq 0.29$ SV.

Fig. 6c shows the PV loop, *i.e.* the ventricular pressure p_{LV} plotted against the volume V_{LV}, which describes the mechanical work performed by the ventricle. The four typical sections of cardiac dynamics can be noticed in this last diagram. First, the isovolumic contraction phase (yellow dotted vertical line) builds up pressure inside the LV with the valves closed. Then, this pressure initiates valve opening (not in our simplified valve model) and leads to the actual ventricular contraction (red dotted horizontal line). This contraction is almost isotonic, apart from the initial slight increase of pressure due to the arterial elasticity after the aortic valve has opened. This systolic contraction is then followed by the closure of the aortic valve and the transition to an isovolumic relaxation phase (purple dotted vertical line). This phase ends with the opening of the mitral valve, which initiates the isotonic filling (green dotted horizontal line) of the ventricle. The cycle ends with the closure of the mitral valve and repeats from the beginning.

The pressure oscillations at each corner are induced by the imposed valve opening and closure timings that are not perfectly matched with the rest of the in-vivo data (see Section 2.1). During the isotonic ejection phase (red dotted line), for example, the aortic valve closes

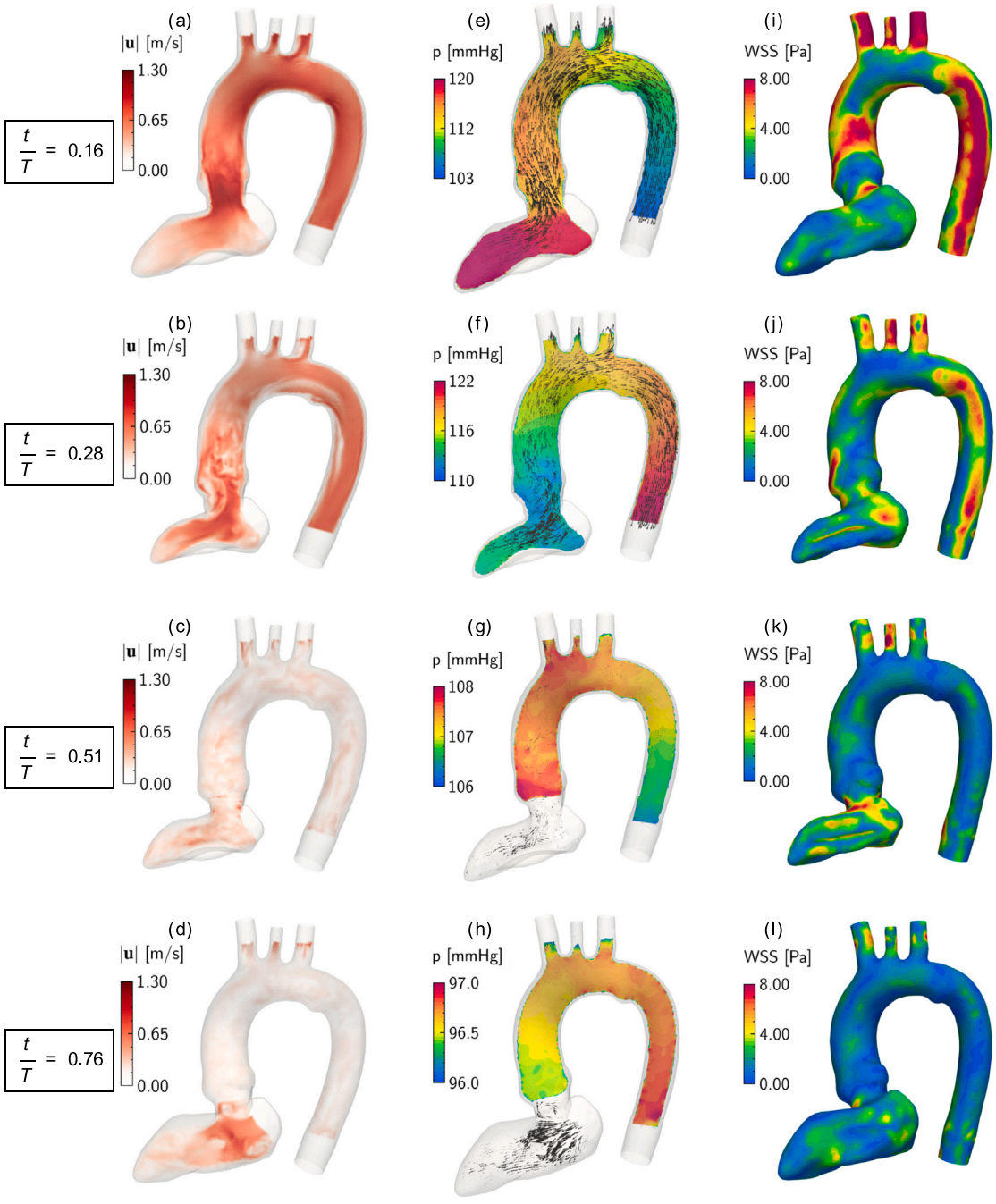

Fig. 7. Blood velocity, pressure and WSS at systolic peak ($t/T = 0.16$), late systole ($t/T = 0.28$), early diastole ($t/T = 0.51$) and late diastole ($t/T = 0.76$). Blood velocity (**a–d**) and pressure (**e–h**) distributions are shown on a longitudinal section of the left ventricle and aorta. Color bar ranges of the pressure are different for each time point in order to appreciate the pressure gradient inside the aorta. Black arrows show the local velocity direction and magnitude.

too early with respect to the in-vivo data, creating a buildup of pressure that disappears as soon as the valve opens (top-left corner of Fig. 6c).

Fig. 7 shows snapshots of blood velocity and pressure distributions on a longitudinal section of the left ventricle and aorta. Additionally, wall shear stress (WSS) is shown on the aortic and ventricular walls. Each quantity is depicted at four typical time points of the cardiac cycle: systolic peak ($t/T = 0.16$), late systole ($t/T = 0.28$), early ($t/T = 0.51$) and late ($t/T = 0.76$) diastole. For the pressure, the color bar scale range is tuned differently for each snapshot in order to highlight the pressure gradient inside the aorta. Additionally, black arrows are drawn in the blood velocity direction in order to visualize flow patterns. At the systolic peak (Fig. 7a,e,i) we can see that the LV contraction has developed and a strong pressure gradient of around 20 mmHg is generated smoothly from the ventricular apex down to the descending aorta.

Fig. 8 shows the blood velocity at the same four time points of Fig. 7, but on the $\pi_1, \ldots, \pi_4$ cross sections of the aorta. The first column of Fig. 8 highlights that the developed flow is almost laminar, especially in the more distal cross sections (Fig. 8e,i,m). A high value of WSS of 8 Pa (Fig. 7i,j) develops in small regions of both the ascending and descending aorta. Particular patterns of high WSS, which last until late systole (Fig. 7j) develop on the descending aorta wall. We assume that these patterns are caused by vortices that develop in correspondence with the small bump on the inferior section of the aortic arch, as can be seen from Figs. 7b and 8j–k. During late systole (Fig. 7b,f,j) the pressure gradient caused by the ventricular contraction has vanished

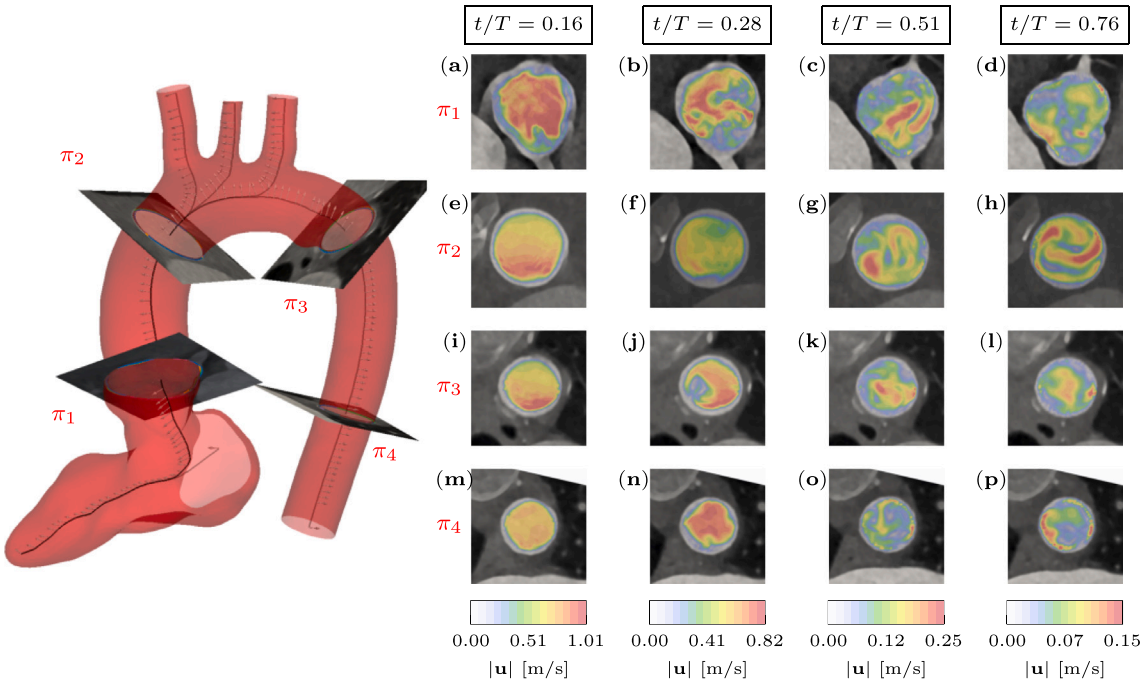

Fig. 8. Blood velocity in cross sections $\pi_1, \ldots, \pi_4$ of the aorta. The sections correspond to the aortic annulus, ascending aorta (just before the aortic arch), and descending aorta (just after the arch and near the end of the simulated domain), respectively. The velocity is plotted at four characteristic time points of the cardiac cycle: systolic peak ($t/T = 0.16$), late systole ($t/T = 0.28$), early diastole ($t/T = 0.51$) and late diastole ($t/T = 0.76$), for each cross-section.

and an inverse gradient starts to build up. However, the blood flow is still propelled by its inertia. At this moment, turbulent flow patterns start to develop due to the break of the almost-laminar configuration of the systolic peak (see also Fig. 8b,j,c,g). Additionally, with the fluid's inertia acting as the main lead of the flow the inlet velocity profile becomes particularly asymmetrical with respect to the aortic annulus (Fig. 7b and 8b–d).

At early diastole (Fig. 7c,g,k), the aortic valve has closed and the mitral valve has recently opened, allowing blood from the atrium to refill the ventricle. Even if velocity has dropped by more than 90% of the systolic values, we can notice that the blood flowrates at the descending aorta (and supra-aortic vessels as well, even if not reported on the plots) are still slightly positive from Fig. 6b. This smaller flowrate is propelled by the aortic compliance $d/dtV_{AO} < 0$ which recreates a (smaller) positive gradient pressure of about 2 mmHg (Fig. 7g) throughout the aorta and maintains a steady flow direction.

At late diastole (Fig. 7d,h,l) the blood flow from the atrium to the ventricle has increased and the ventricle is almost filled up completely. Interestingly, vortices can be observed inside the ventricle. The pressure gradient inside the aorta has decreased to almost zero (around 1 mmHg) and the cardiac cycle is almost to its end.

3.4. Footprint of the periaortic structures in the nudging forces

This section examines the spatial distribution of nudging forces on the aorta to identify potential interactions with periaortic structures. DENSE MRI (Displacement Encoding with Stimulated Echoes Magnetic Resonance Imaging) studies [87] have shown that the aorta's displacement and deformation are heterogeneous and it has been suggested that these variations may be partially due to the influence of periaortic interactions [88]. Given the patient-specific nature of these interactions and the challenges in accurately modeling them, a data-driven approach like nudging offers a promising solution.

To this aim, Fig. 9 illustrates the spatial distribution of surface-orthogonal nudging forces, defined as

$$f_{i\perp}^{N(P)} = \mathbf{n}_i \cdot \mathbf{f}_i^{N(P)} \tag{13}$$

on the aorta during early systole, where $\mathbf{n}_i$ is the outward facing normal of each mesh vertex. The figure also depicts in shaded gray the configuration of periaortic structures surrounding the heart and aorta, as extracted from the CT scan.

The spatial distribution of the orthogonal nudging forces manifest several local maxima of $f_{i\perp}^{N(P)}$ in regions where the aorta is in proximity to key periaortic structures, as highlighted by arrows in the figure. These periaortic interactions act as constraints on the cardiovascular system, and their effect may be partially captured by the nudging forces. For instance, a peak of $f_{i\perp}^{N(P)}$ is present near the contact point between the ascending aorta and the pulmonary artery, suggesting additional pressure exerted by the pulmonary artery on the aorta. Similarly, two other peaks are observed at the contact points between the aorta and the superior vena cava, and the right atrium. Additionally, a ring-shaped maximum of $f_{i\perp}^{N(P)}$ can be seen around the aortic annulus, likely reflecting the oscillatory motion of the heart, driven by myocardial contraction, that causes a similar motion in the aorta. Finally, the local maxima found around supraortic vessels likely reflect the constraining action of structures inside the suprasternal area, such as the esophagus or the trachea.

4. Discussion

In this work, an FSI-based computational model of the cardiovascular segment was created using dynamic imaging data to "guide" the simulation toward in-vivo information. On one hand, the mathematical laws governing blood flow and soft tissue deformations are numerically solved to obtain a physical characterization of the system. On the other hand, the in-vivo measurements from a dynamic CT Angiography scan are incorporated into the model to improve its predictions and enhance its patient-specificity. This is done through Data Assimilation using an algorithm inspired by Nudging. The study demonstrates that nudging integral measurements over time, such as LV volume and area, can accurately reproduce the main ventricular functional parameters without needing a comprehensive electrophysiological model (Table 2). This is significant as such measurements are readily obtainable via non-invasive imaging techniques like echocardiography [81–83].

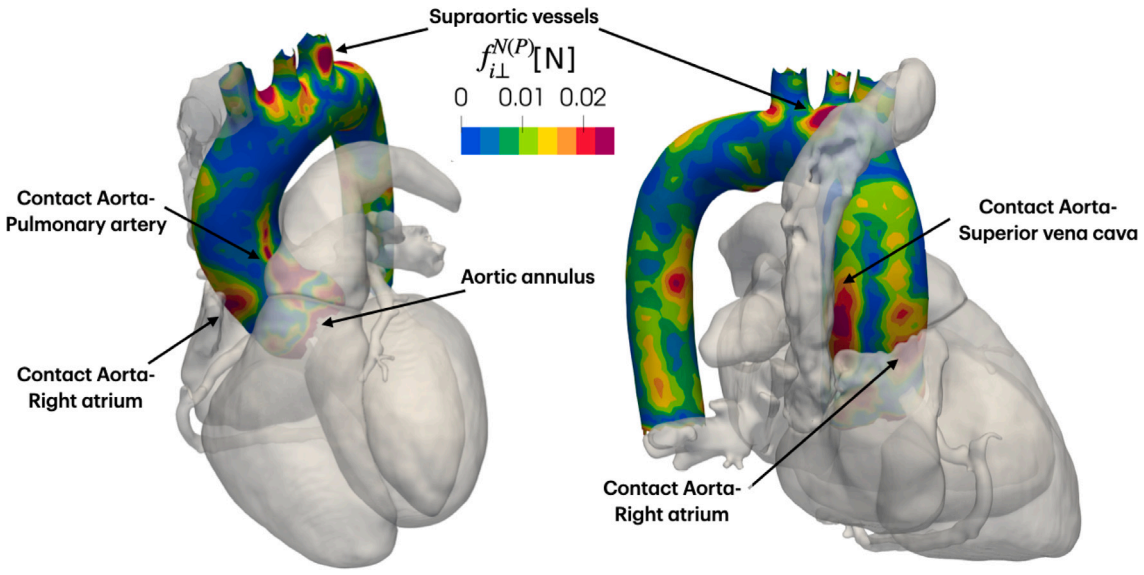

Fig. 9. Spatial distribution of surface-orthogonal nudging forces $f_{i\perp}^{N(P)}$ on the aorta during early systole, with periaortic structures extracted from the CT scan. Contact regions where the aorta is in proximity to periaortic structures are highlighted with arrows. These regions seem to correspond to local maxima of the nudging force.

Additionally, the study highlights that, despite the superior morphological detail from CT scans, segmentation of the left ventricle is prone to noise due to complex multi-scale irregularities of the myocardium. This is caused by the presence of small-scale structures such as papillary muscles, cordae tendinae and trabeculae (bottom green arrow in Fig. 1a). Therefore, the proposed method suggests initially assimilating integral variables to match functional parameters closely and then incrementally incorporating local measurements based on noise levels. Indeed, in order to achieve higher fidelity of the ventricular kinematics, additional local measurements are necessary, as detailed in Section 3.1 and Fig. 3 where this possibility is explored by nudging also the Lagrangian positions and displacements. In contrast to the ventricular region, nudging of integral variables was unnecessary for the aorta due to two reasons. Firstly, the in-silico model was capable of replicating integral quantities like aortic compliance ($\Delta\hat{V}_{AO}$) effectively even with very low nudging intensities (Fig. 4 panels a,b,c,d). Secondly, the high-quality images used in the study facilitated faster and more accurate aortic lumen segmentations (top green arrow in Fig. 1a). These findings indicate that the need for nudging may vary depending on the imaging modality and its limitations.

To improve the efficacy of Nudging Lagrangian position measurements (local variables), the accuracy of the normal and tangential components of the displacements (with respect to the lumen boundary) should be considered. In Chabiniok et al. [20], for example, they use a signed distance field with respect to the lumen boundary, thus eliminating any tangential component of the displacements. On the other hand, employing a different imaging technique (probably in the near future, with higher temporal and spatial resolution) and registration procedure, could enable the integration of patient-specific tangential material point displacements. This data could contain relevant physiological information such as the myocardium helical contraction patterns or more detailed orthotropic material strains. This information would easily be incorporated into the assimilation process without requiring modifications to the algorithm or computational framework (through the point-wise forces $\mathbf{f}_i^{N(P)}$).

Clinically, obtaining time-dependent Lagrangian positions of cardiac structures is more time consuming and requires more invasive techniques (like CT in this study) compared to simple volumetric and area measurements. However, advancements in medical imaging technology are continually enhancing the diagnostic capabilities and safety of modalities like CT, making comprehensive imaging increasingly accessible [14–17]. Moreover, the rapid development of Artificial Intelligence in medical imaging analysis can facilitate quicker data processing and reduce intra/inter-observer variability of the results [89–91]. The latter study, specifically, employs neural networks to fit template cardiac meshes to MRI image data and directly obtain material point displacements and meshes suitable for numerical simulations.

This research leverages high-quality CT data for its rich morphological detail [14–17], focusing the DA process on structural information of soft tissues. Indeed, CT allows accurate measurements of boundary lumen deformations given its higher spatial resolution. Conversely, modalities like 4D-Flow cardiovascular magnetic resonance [92] could provide flow measurements and allow DA of fluid dynamics as well [28,93,94]. Specifically, the nudging algorithm is well studied in fluid dynamics [36,79] and recently in turbulence as well [35,95]. This would come at the cost of a reduced spatial resolution and contrast, even though a segmentation of the structures remains possible, as demonstrated in Bustamante et al. [96], Garzia et al. [60], Berhane et al. [97].

In general, the success of the reconstruction (the results of the "guided" simulation) will depend on the amount of information provided (how many measurements in space and in time), on its quality (where and what we measure), and on the nudging intensity itself. In principle, this intensity should be very large, provided that the in-vivo measurements are perfect (zero noise) and compatible with the simplifications of the model. However, as observed in Fig. 4, imposing the in-vivo kinematics with high intensity (experiments NA3 and NA4) amplifies inconsistencies between the measurements and the model. In fact, the right intensity must be calibrated such that the system remains inside the measurement uncertainty range and should not be any higher to avoid these unwanted effects. It is intuitive to imagine that, in some cases, it might be better to allow for a larger error in some small regions to allow the system to be closer to the target globally and obtain more physical results. Moreover, the driving in-vivo kinematics is interpolated in time at every numerical time step, which is much smaller than the time resolution of the CT scan (33 ms). A too strong nudging would thus produce a non-realistic evolution of the simulation.

To reduce this effect, Moireau et al. [26], Bertoglio et al. [27] proposed to introduce nudging as correction to the velocity–displacement relation, rather than as a force applied on the mechanical system. This approach ensures that the correction term maintains a dissipative nature without increasing the system's rigidity.

It is evident that determining the optimal nudging intensity is crucial. However, a robust methodology for determining the right balance

still remains uncertain. We plan to apply the proposed method in a context where both structural and hemodynamic data are perfectly known (numerical mock setup) to verify the accuracy of the reconstructed fields.

Additionally, we plan to utilize a more comprehensive cardiac anatomy, including each of the four chambers and the principal artery/veins of the cardiovascular system, along with a detailed FSI model of the valves. This would eliminate the spurious effects in the PV loop of Fig. 6c that are due to slightly erroneous opening and closing timings of the valves and their simplified dynamics. Although an initial tuning of the valve timings was performed in order to reduce these bumps, a precise modeling of the valves is essential for accurately reproducing such diagrams. A key advantage of the implemented nudging strategy is its simplicity and general applicability. It does not rely on the specific assumptions used in this work and can be applied to more complex cardiac models. For instance, it can cope with more detailed cardiac anatomies, also including cardiac valves and the orthotropic nature of the myocardium.

Finally, other kinds of Data Assimilation algorithms (such as reduced Kalman filters [18,78] or other variational DA techniques [23]) can be studied to evaluate their performance and test their applicability to complex FSI simulations like the one explored in this work.

CRediT authorship contribution statement

Martino Andrea Scarpolini: Writing – review & editing, Writing – original draft, Software, Methodology, Investigation, Data curation, Conceptualization. **Giulia Piumini:** Software, Methodology, Conceptualization. **Emanuele Gasparotti:** Writing – review & editing, Methodology, Data curation, Conceptualization. **Erica Maffei:** Resources, Data curation, Conceptualization. **Filippo Cademartiri:** Resources, Data curation, Conceptualization. **Simona Celi:** Writing – review & editing, Supervision, Methodology, Data curation, Conceptualization. **Francesco Viola:** Writing – review & editing, Supervision, Software, Methodology, Investigation, Conceptualization.

Declaration of competing interest

None Declared.

Acknowledgments

We acknowledge useful discussion with Luca Biferale about the application of Nudging. The authors thank Roberto Verzicco for several discussions on the computational aspects of the problem. This project is carried on in the framework of the MeDiTaTe Project, which has received funding from the European Union's Horizon 2020 research and innovation programme under Grant Agreement 859836. This project has received funding from the European Research Council (ERC) under the European Union's Horizon Europe research and innovation program (Grant No. 101039657, CARDIOTRIALS to F.V.). This work has received partial funding from the project MUR-FARE R2045J8XAW CUP E83C22005500001 (P.I. Luca Biferale).

Appendix A. Stress-free geometry computation

The soft tissue dynamics is described in Section 2.4. The initial conditions of the structural mesh are initialized from the in-vivo model in order to obtain anatomical personalization of the cardiac structures. However, $\hat{\mathbf{y}}(t_0)$ is associated with the in-vivo end-diastolic configuration, *i.e.*, to a non-stress-free state for the aorta, with a typical arterial pressure of 80 mmHg. Consequently, $\hat{\mathbf{y}}(t_0)$ corresponds to a pressurized configuration and not to a stress-free one. To start the simulation accounting for this initial "pre-stress", a stress-free configuration must be estimated. This consists of an inverse problem where the final result of the pressurization is known (the diastolic configuration), and the initial configuration must be computed. The real pressure distribution along the walls should also be known to estimate this configuration accurately. However, in our work, we acquired patient-specific data solely from the CT scan, and consequently, the pressure load is unknown. Therefore, we assume a homogeneous physiological diastolic pressure of 80 mmHg and use the weighted reverse displacement method [73,74] to find the stress-free configuration of the aortic walls. In this procedure, the endocardium is not considered as it is assumed to be in its unstressed configuration. The aortic wall described by $\hat{\mathbf{y}}(t_0)$, instead, is inflated to 80 mmHg to obtain an estimation of the displacement of each vertex of the structure under pressure. The over-inflated geometry is described by the positions $\hat{\mathbf{y}}^{80}(t_0)$ and the displacements are given by

$$\delta\mathbf{y}^{0\mapsto 80} = \hat{\mathbf{y}}^{80}(t_0) - \hat{\mathbf{y}}(t_0). \tag{14}$$

These displacements are then used to estimate the stress-free configuration $\hat{\mathbf{y}}^{0}(t_0)$ by inverting the sign and adding a multiplicative correction factor α:

$$\hat{\mathbf{y}}^{0}(t_0) = \hat{\mathbf{y}}(t_0) - \alpha \cdot \delta\mathbf{y}^{0\mapsto 80} \tag{15}$$

The correct value of α is selected by re-inflating the obtained geometry $\hat{\mathbf{y}}^{0}(t_0)$ to 80 mmHg and checking the vertex-to-vertex distance with respect to the in-vivo end-diastolic geometry $\hat{\mathbf{y}}(t_0)$. Typically, values of $\alpha \simeq 0.8$ allow to reach the minimum distance. The final geometry $\hat{\mathbf{y}}^{0}(t_0)$ obtained with the correct α is used as the initial conditions of the structural mesh of the simulation.

Appendix B. Estimation of nudging coefficients

Selecting appropriate parameters for sequential data assimilation methods, such as nudging, can be computationally demanding, particularly when the model requires significant computational efforts to be numerically integrated. This appendix provides two examples for estimating the order of magnitude of two nudging parameters used in this study: k_A for the left ventricle and k_P for the aorta. These rough estimates are derived from the system's physical constants.

To effectively correct the dynamics, referring to Eq. (5), the nudging force $\mathbf{f}^N$ must be comparable to the hydrodynamic forces $\mathbf{f}^H$ or internal structural forces $\mathbf{f}^I$ acting on the system.

For the left ventricle, where the active stress is predominantly balanced by internal structural forces, the nudging parameter estimation is based on the stiffness of the structure. The surface area force $\mathbf{f}^{N(A)}$, responsible for counteracting elastic stiffness, can be expressed as

$$\left\|\mathbf{f}^{N(A)}\right\| = k_A \left(\frac{A-\hat{A}}{\hat{A}}\right) \left\|\frac{\partial A}{\partial \mathbf{y}}\right\| \sim k_A \left(\frac{A-\hat{A}}{\hat{A}}\right) \frac{l}{2}$$

where l is the average edge length of the structural mesh and $\partial A/\partial \mathbf{y}$ is computed as in Krüger [80]. The internal force is given by

$$\left\|\mathbf{f}^{I}\right\| \sim Eh \left(\frac{l-l_0}{l_0}\right) l_0$$

where l_0 is the average stress-free edge length of the structural mesh, E the elastic modulus and h the thickness of the structure, as described in de Tullio and Pascazio [53]. Assuming a maximum strain $(l-l_0)/l_0 \simeq 0.5$ during systole and imposing a maximum discrepancy of 5% relative to measurement data, the equation for k_A (expressing each quantity using nondimensional units) becomes:

$$\left\|\mathbf{f}^{N(A)}\right\| \simeq \left\|\mathbf{f}^{I}\right\| \quad \Longrightarrow \quad k_A \sim \frac{2Eh\left(\frac{l-l_0}{l_0}\right) l_0}{l\left(\frac{A-\hat{A}}{\hat{A}}\right)} \sim 800$$

This value is in close agreement with the values chosen for NLV2 and NLV3 (1000).

For the aorta, where the dynamics is passive and predominantly governed by the hydrodynamic loads $\mathbf{f}^H$, a reasonable estimate for the nudging constant k_P is given by comparing the hydrodynamic loads with the point-wise nudging force

$$\left\|\mathbf{f}^{N(P)}\right\| \simeq k_P \left\|\mathbf{y}-\hat{\mathbf{y}}\right\|_{\text{av}}, \qquad \left\|\mathbf{f}^{H}\right\| \simeq p_{\text{dia}} A_{\text{av}}$$

where p_{dia} is the average diastolic pressure (approximately 80 mmHg), A_{av} is the average area of the structural mesh elements, and $\|y - \hat{y}\|_{\text{av}}$ represents the maximum average discrepancy between in-silico and in vivo data tolerated. Setting $\|y - \hat{y}\|_{\text{av}} = 0.11$ mm, *i.e.* the measurement error in material point positions, we obtain (expressing each quantity using nondimensional units):

$$\left\|\mathbf{f}^N\right\| \simeq \left\|\mathbf{f}^H\right\| \quad \Longrightarrow \quad k_P \sim p_{dia} A_{\text{av}} / \|y - \hat{y}\|_{\text{av}} \simeq 12$$

This value closely matches the choice made for experiment NA3 (10).

References

[1] R. Verzicco, Electro-fluid-mechanics of the heart, J. Fluid Mech. 941 (2022) P1.

[2] F. Viola, V. Meschini, R. Verzicco, Fluid–structure-electrophysiology interaction (FSEI) in the left-heart: a multi-way coupled computational model, Eur. J. Mech. B Fluids 79 (2020) 212–232.

[3] F. Viola, V. Spandan, V. Meschini, J. Romero, M. Fatica, M.D. de Tullio, R. Verzicco, FSEI-GPU: GPU accelerated simulations of the fluid–structure–electrophysiology interaction in the left heart, Comput. Phys. Comm. 273 (2022) 108248.

[4] F. Sturla, E. Votta, M. Stevanella, C.A. Conti, A. Redaelli, Impact of modeling fluid–structure interaction in the computational analysis of aortic root biomechanics, Med. Eng. Phys. 35 (12) (2013) 1721–1730.

[5] M. Bucelli, A. Zingaro, P.C. Africa, I. Fumagalli, L. Dede', A. Quarteroni, A mathematical model that integrates cardiac electrophysiology, mechanics, and fluid dynamics: Application to the human left heart, Int. J. Numer. Methods Biomed. Eng. 39 (3) (2023) e3678.

[6] M. Fedele, R. Piersanti, F. Regazzoni, M. Salvador, P.C. Africa, M. Bucelli, A. Zingaro, A. Quarteroni, et al., A comprehensive and biophysically detailed computational model of the whole human heart electromechanics, Comput. Methods Appl. Mech. Engrg. 410 (2023) 115983.

[7] L. Feng, H. Gao, X. Luo, Whole-heart modelling with valves in a fluid–structure interaction framework, Comput. Methods Appl. Mech. Engrg. 420 (2024) 116724.

[8] A. Santiago, J. Aguado-Sierra, M. Zavala-Aké, R. Doste-Beltran, S. Gómez, R. Arís, J.C. Cajas, E. Casoni, M. Vázquez, Fully coupled fluid-electro-mechanical model of the human heart for supercomputers, Int. J. Numer. Methods Biomed. Eng. 34 (12) (2018) e3140.

[9] N. Benameur, E.G. Caiani, Y. Arous, N. Ben Abdallah, T. Kraiem, Parametric imaging for the assessment of cardiac motion: a review, Cardiovasc. Eng. Technol. 9 (2018) 377–393.

[10] C. Bertoglio, P. Moireau, J.F. Gerbeau, Sequential parameter estimation for fluid–structure problems: application to hemodynamics, Int. J. Numer. Methods Biomed. Eng. 28 (4) (2012) 434–455.

[11] D. Nolte, C. Bertoglio, Inverse problems in blood flow modeling: A review, Int. J. Numer. Methods Biomed. Eng. 38 (8) (2022) e3613.

[12] R. Chabiniok, V.Y. Wang, M. Hadjicharalambous, L. Asner, J. Lee, M. Sermesant, E. Kuhl, A.A. Young, P. Moireau, M.P. Nash, et al., Multiphysics and multiscale modelling, data–model fusion and integration of organ physiology in the clinic: ventricular cardiac mechanics, Interface Focus. 6 (2) (2016) 20150083.

[13] S. Celi, N. Martini, L. Emilio Pastormerlo, V. Positano, S. Berti, Multimodality imaging for interventional cardiology, Curr. Pharm. Des. 23 (22) (2017) 3285–3300.

[14] H. Schoellnast, M. Tillich, M.J. Deutschmann, H.A. Deutschmann, G.J. Schaffler, H.R. Portugaller, Aortoiliac enhancement during computed tomography angiography with reduced contrast material dose and saline solution flush: influence on magnitude and uniformity of the contrast column, Invest. Radiol. 39 (1) (2004) 20–26.

[15] S.T. Schindera, P. Graca, M.A. Patak, S. Abderhalden, G. von Allmen, P. Vock, Z. Szucs-Farkas, Thoracoabdominal-aortoiliac multidetector-row CT angiography at 80 and 100 kVp: assessment of image quality and radiation dose, Invest. Radiol. 44 (10) (2009) 650–655.

[16] B. Wintersperger, T. Jakobs, P. Herzog, S. Schaller, K. Nikolaou, C. Suess, C. Weber, M. Reiser, C. Becker, Aorto-iliac multidetector-row CT angiography with low kV settings: improved vessel enhancement and simultaneous reduction of radiation dose, Eur. Radiol. 15 (2005) 334–341.

[17] A. Meloni, F. Cademartiri, V. Positano, S. Celi, S. Berti, A. Clemente, L. La Grutta, L. Saba, E. Bossone, C. Cavaliere, et al., Cardiovascular applications of photon-counting CT technology: A revolutionary new diagnostic step, J. Cardiovasc. Dev. Dis. 10 (9) (2023) 363.

[18] P. Moireau, D. Chapelle, P. Le Tallec, Joint state and parameter estimation for distributed mechanical systems, Comput. Methods Appl. Mech. Engrg. 197 (6–8) (2008) 659–677.

[19] G. Li, D. Citrin, K. Camphausen, B. Mueller, C. Burman, B. Mychalczak, R.W. Miller, Y. Song, Advances in 4D medical imaging and 4D radiation therapy, Technol. Cancer Res. Treat. 7 (1) (2008) 67–81.

[20] R. Chabiniok, P. Moireau, P.-F. Lesault, A. Rahmouni, J.-F. Deux, D. Chapelle, Estimation of tissue contractility from cardiac cine-MRI using a biomechanical heart model, Biomech. Model. Mechanobiol. 11 (2012) 609–630.

[21] S. Celi, E. Gasparotti, K. Capellini, F. Bardi, M.A. Scarpolini, C. Cavaliere, F. Cademartiri, E. Vignali, An image-based approach for the estimation of arterial local stiffness in vivo, Front. Bioeng. Biotechnol. (ISSN: 2296-4185) 11 (2023).

[22] C.T. Metz, S. Klein, M. Schaap, T. van Walsum, W.J. Niessen, Nonrigid registration of dynamic medical imaging data using nD+ t B-splines and a groupwise optimization approach, Med. Image Anal. 15 (2) (2011) 238–249.

[23] M. D'Elia, L. Mirabella, T. Passerini, M. Perego, M. Piccinelli, C. Vergara, A. Veneziani, Applications of variational data assimilation in computational hemodynamics, Model. Physiol. Flows (2012) 363–394.

[24] P. Moireau, C. Bertoglio, N. Xiao, C.A. Figueroa, C. Taylor, D. Chapelle, J.-F. Gerbeau, Sequential identification of boundary support parameters in a fluid-structure vascular model using patient image data, Biomech. Model. Mechanobiol. 12 (2013) 475–496.

[25] M. Asch, M. Bocquet, M. Nodet, Data Assimilation: Methods, Algorithms, and Applications, SIAM, 2016.

[26] P. Moireau, D. Chapelle, P. Le Tallec, Filtering for distributed mechanical systems using position measurements: perspectives in medical imaging, Inverse Problems 25 (3) (2009) 035010.

[27] C. Bertoglio, D. Chapelle, M.A. Fernández, J.-F. Gerbeau, P. Moireau, State observers of a vascular fluid–structure interaction model through measurements in the solid, Comput. Methods Appl. Mech. Engrg. 256 (2013) 149–168.

[28] J. Garay, D. Nolte, M. Löcke, C. Bertoglio, Parameter estimation in fluid flow models from aliased velocity measurements, Inverse Problems 38 (9) (2022) 095002.

[29] C. Bertoglio, D. Barber, N. Gaddum, I. Valverde, M. Rutten, P. Beerbaum, P. Moireau, R. Hose, J.F. Gerbeau, Identification of artery wall stiffness: In vitro validation and in vivo results of a data assimilation procedure applied to a 3D fluid–structure interaction model, J. Biomech. 47 (5) (2014) 1027–1034.

[30] P. Moireau, N. Xiao, M. Astorino, C.A. Figueroa, D. Chapelle, C.A. Taylor, J.-F. Gerbeau, External tissue support and fluid–structure simulation in blood flows, Biomech. Model. Mechanobiol. 11 (2012) 1–18.

[31] D. Chapelle, N. Cîndea, P. Moireau, Improving convergence in numerical analysis using observers—the wave-like equation case, Math. Models Methods Appl. Sci. 22 (12) (2012) 1250040.

[32] L. Bennati, C. Vergara, V. Giambruno, I. Fumagalli, A.F. Corno, A. Quarteroni, G. Puppini, G.B. Luciani, An image-based computational fluid dynamics study of mitral regurgitation in presence of prolapse, Cardiovasc. Eng. Technol. 14 (3) (2023) 457–475.

[33] E. Karabelas, S. Longobardi, J. Fuchsberger, O. Razeghi, C. Rodero, M. Strocchi, R. Rajani, G. Haase, G. Plank, S. Niederer, Global sensitivity analysis of four chamber heart hemodynamics using surrogate models, IEEE Trans. Biomed. Eng. 69 (10) (2022) 3216–3223.

[34] V. Mihalef, R.I. Ionasec, P. Sharma, B. Georgescu, I. Voigt, M. Suehling, D. Comaniciu, Patient-specific modelling of whole heart anatomy, dynamics and haemodynamics from four-dimensional cardiac CT images, Interface Focus. 1 (3) (2011) 286–296.

[35] P.C. Di Leoni, A. Mazzino, L. Biferale, Synchronization to big data: Nudging the Navier-Stokes equations for data assimilation of turbulent flows, Phys. Rev. X 10 (1) (2020) 011023.

[36] J. Blum, F.X. Le Dimet, I.M. Navon, Data assimilation for geophysical fluids, in: Handbook of Numerical Analysis, vol. 14, Elsevier, 2009, pp. 385–441.

[37] A. Fedorov, R. Beichel, J. Kalpathy-Cramer, J. Finet, J.C. Fillion-Robin, S. Pujol, C. Bauer, D. Jennings, F. Fennessy, M. Sonka, et al., 3D slicer as an image computing platform for the quantitative imaging network, Magn. Reson. Imaging 30 (9) (2012) 1323–1341.

[38] Autodesk, inc., Meshmixer, 2018, URL: www.meshmixer.com/.

[39] D.L. Hill, P.G. Batchelor, M. Holden, D.J. Hawkes, Medical image registration, Phys. Med. Biol. 46 (3) (2001) R1.

[40] C.T. Metz, S. Klein, M. Schaap, T. van Walsum, W.J. Niessen, Nonrigid registration of dynamic medical imaging data using nD+ t B-splines and a groupwise optimization approach, Med. Image Anal. 15 (2) (2011) 238–249.

[41] M.A. Scarpolini, M. Mazzoli, S. Celi, Enabling supra-aortic vessels inclusion in statistical shape models of the aorta: a novel non-rigid registration method, Front. Physiol. (ISSN: 1664-042X) 14 (2023).

[42] A. Lembcke, P.M. Dohmen, M. Dewey, C. Klessen, T. Elgeti, K.G.A. Hermann, W.F. Konertz, B. Hamm, D.E. Kivelitz, Multislice computed tomography for preoperative evaluation of right ventricular volumes and function: comparison with magnetic resonance imaging, Ann. Thorac. Surg. 79 (4) (2005) 1344–1351.

[43] F. Grothues, J.C. Moon, N.G. Bellenger, G.S. Smith, H.U. Klein, D.J. Pennell, Interstudy reproducibility of right ventricular volumes, function, and mass with cardiovascular magnetic resonance, Am. Heart J. 147 (2) (2004) 218–223.

[44] E. Maffei, G. Messalli, C. Martini, K. Nieman, O. Catalano, A. Rossi, S. Seitun, A.I. Guaricci, C. Tedeschi, N.R. Mollet, et al., Left and right ventricle assessment with Cardiac CT: validation study vs. Cardiac MR, Eur. Radiol. 22 (2012) 1041–1049.

[45] G. Aoyama, L. Zhao, S. Zhao, X. Xue, Y. Zhong, H. Yamauchi, H. Tsukihara, E. Maeda, K. Ino, N. Tomii, et al., Automatic aortic valve cusps segmentation from CT images based on the cascading multiple deep neural networks, J. Imag. 8 (1) (2022) 11.

[46] M. Handke, G. Heinrichs, F. Beyersdorf, M. Olschewski, C. Bode, A. Geibel, In vivo analysis of aortic valve dynamics by transesophageal 3-dimensional echocardiography with high temporal resolution, J. Thorac. Cardiovasc. Surg. 125 (6) (2003) 1412–1419.
[47] C.E. Eckert, B. Zubiate, M. Vergnat, J.H. Gorman, R.C. Gorman, M.S. Sacks, In vivo dynamic deformation of the mitral valve annulus, Ann. Biomed. Eng. 37 (2009) 1757–1771.
[48] E. Votta, T.B. Le, M. Stevanella, L. Fusini, E.G. Caiani, A. Redaelli, F. Sotiropoulos, Toward patient-specific simulations of cardiac valves: state-of-the-art and future directions, J. Biomech. 46 (2) (2013) 217–228.
[49] D. Katritsis, L. Kaiktsis, A. Chaniotis, J. Pantos, E.P. Efstathopoulos, V. Marmarelis, Wall shear stress: theoretical considerations and methods of measurement, Prog. Cardiovasc. Dis. 49 (5) (2007) 307–329.
[50] F. De Vita, M.D. de Tullio, R. Verzicco, Numerical simulation of the blood flow in the aortic root with a non-newtonian fluid model, in: AIMETA Conference, 2013, pp. 1–8.
[51] R. Verzicco, P. Orlandi, A finite-difference scheme for three-dimensional incompressible flows in cylindrical coordinates, J. Comput. Phys. 123 (2) (1996) 402–414.
[52] E.P. Van Der Poel, R. Ostilla-Mónico, J. Donners, R. Verzicco, A pencil distributed finite difference code for strongly turbulent wall-bounded flows, Comput. & Fluids 116 (2015) 10–16.
[53] M.D. de Tullio, G. Pascazio, A moving-least-squares immersed boundary method for simulating the fluid–structure interaction of elastic bodies with arbitrary thickness, J. Comput. Phys. 325 (2016) 201–225.
[54] V. Spandan, V. Meschini, R. Ostilla-Mónico, D. Lohse, G. Querzoli, M.D. de Tullio, R. Verzicco, A parallel interaction potential approach coupled with the immersed boundary method for fully resolved simulations of deformable interfaces and membranes, J. Comput. Phys. 348 (2017) 567–590.
[55] V. Spandan, D. Lohse, M.D. de Tullio, R. Verzicco, A fast moving least squares approximation with adaptive Lagrangian mesh refinement for large scale immersed boundary simulations, J. Comput. Phys. 375 (2018) 228–239.
[56] N. Westerhof, J.W. Lankhaar, B.E. Westerhof, The arterial windkessel, Med. Biol. Eng. Comput. 47 (2) (2009) 131–141.
[57] A. Boccadifuoco, A. Mariotti, S. Celi, N. Martini, M. Salvetti, Impact of uncertainties in outflow boundary conditions on the predictions of hemodynamic simulations of ascending thoracic aortic aneurysms, Comput. & Fluids 165 (2018) 96–115.
[58] R.M. Romarowski, A. Lefieux, S. Morganti, A. Veneziani, F. Auricchio, Patient-specific CFD modelling in the thoracic aorta with PC-MRI–based boundary conditions: A least-square three-element windkessel approach, Int. J. Numer. Methods Biomed. Eng. 34 (11) (2018) e3134.
[59] P. Youssefi, A. Gomez, C. Arthurs, R. Sharma, M. Jahangiri, C. Alberto Figueroa, Impact of patient-specific inflow velocity profile on hemodynamics of the thoracic aorta, J. Biomech. Eng. 140 (1) (2018) 011002.
[60] S. Garzia, M.A. Scarpolini, M. Mazzoli, K. Capellini, A. Monteleone, F. Cademartiri, V. Positano, S. Celi, Coupling synthetic and real-world data for a deep learning-based segmentation process of 4D flow MRI, Comput. Methods Programs Biomed. 242 (2023) 107790.
[61] K. Capellini, E. Gasparotti, U. Cella, E. Costa, B.M. Fanni, C. Groth, S. Porziani, M.E. Biancolini, S. Celi, A novel formulation for the study of the ascending aortic fluid dynamics with in vivo data, Med. Eng. Phys. 91 (2021) 68–78.
[62] R. Storn, K. Price, Differential evolution–a simple and efficient heuristic for global optimization over continuous spaces, J. Global Optim. 11 (4) (1997) 341–359.
[63] M.N. Antonuccio, A. Mariotti, B.M. Fanni, K. Capellini, C. Capelli, E. Sauvage, S. Celi, Effects of uncertainty of outlet boundary conditions in a patient-specific case of aortic coarctation, Ann. Biomed. Eng. 49 (12) (2021) 3494–3507.
[64] D.A. Fedosov, B. Caswell, G.E. Karniadakis, Systematic coarse-graining of spectrin-level red blood cell models, Comput. Methods Appl. Mech. Engrg. 199 (29–32) (2010) 1937–1948.
[65] P.E. Hammer, M.S. Sacks, P.J. Del Nido, R.D. Howe, Mass-spring model for simulation of heart valve tissue mechanical behavior, Ann. Biomed. Eng. 39 (2011) 1668–1679.
[66] G. Holzapfel, Biomechanics of soft tissue, in: The Handbook of Materials Behavior Models, Academic Press, 2001, pp. 1049–1063.
[67] J.P. Jehl, P. Dan, A. Voignier, N. Tran, T. Bastogne, P. Maureira, F. Cleymand, Transverse isotropic modelling of left-ventricle passive filling: Mechanical characterization for epicardial biomaterial manufacturing, J. Mech. Behav. Biomed. Mater. 119 (2021) 104492.
[68] C.Y. Liu, D. Chen, D.A. Bluemke, C.O. Wu, G. Teixido-Tura, A. Chugh, S. Vasu, J.A. Lima, W.G. Hundley, Evolution of aortic wall thickness and stiffness with atherosclerosis: long-term follow up from the multi-ethnic study of atherosclerosis, Hypertension 65 (5) (2015) 1015–1019.
[69] W. Grossman, L.P. Mclaurin, S.P. Moos, M. Stefadouros, D.T. Young, Wall thickness and diastolic properties of the left ventricle, Circulation 49 (1) (1974) 129–135.
[70] J.W. Kennedy, W.A. Baxley, M.M. Figley, H.T. Dodge, J.R. Blackmon, Quantitative angiocardiography: I. The normal left ventricle in man, Circulation 34 (2) (1966) 272–278.
[71] F. Viola, G. Del Corso, R. De Paulis, R. Verzicco, GPU accelerated digital twins of the human heart open new routes for cardiovascular research, Sci. Rep. 13 (1) (2023) 8230.
[72] G. Del Corso, R. Verzicco, F. Viola, A fast computational model for the electrophysiology of the whole human heart, J. Comput. Phys. 457 (2022) 111084.
[73] M. Raghavan, B. Ma, M.F. Fillinger, Non-invasive determination of zero-pressure geometry of arterial aneurysms, Ann. Biomed. Eng. 34 (2006) 1414–1419.
[74] E. Vignali, E. Gasparotti, S. Celi, S. Avril, Fully-coupled FSI computational analyses in the ascending thoracic aorta using patient-specific conditions and anisotropic material properties, Front. Physiol. (ISSN: 1664-042X) 12 (2021).
[75] A. Stuart, K. Zygalakis, Data Assimilation: A Mathematical Introduction, Technical Report, Oak Ridge National Lab.(ORNL), Oak Ridge, TN (United States), 2015.
[76] H.D. Abarbanel, The Statistical Physics of Data Assimilation and Machine Learning, Cambridge University Press, 2022.
[77] G. Welch, G. Bishop, et al., An Introduction to the Kalman Filter, Citeseer, 1995.
[78] P. Moireau, D. Chapelle, Reduced-order unscented Kalman filtering with application to parameter identification in large-dimensional systems, ESAIM Control Optim. Calc. Var. 17 (2) (2011) 380–405.
[79] L. Agasthya, P. Clark Di Leoni, L. Biferale, Reconstructing Rayleigh–Bénard flows out of temperature-only measurements using nudging, Phys. Fluids 34 (1) (2022).
[80] H. Krüger, Computer Simulation Study of Collective Phenomena in Dense Suspensions of Red Blood Cells Under Shear, Springer Science & Business Media, 2012.
[81] M.I. Levene, Measurement of the growth of the lateral ventricles in preterm infants with real-time ultrasound, Arch. Dis. Child. 56 (12) (1981) 900–904.
[82] H. Feigenbaum, A. Zaky, W.K. Nasser, C.L. Haine, Use of ultrasound to measure left ventricular stroke volume, Circulation 35 (6) (1967) 1092–1099.
[83] G. Carneiro, J. Nascimento, A. Freitas, Robust left ventricle segmentation from ultrasound data using deep neural networks and efficient search methods, in: 2010 IEEE International Symposium on Biomedical Imaging: From Nano to Macro, IEEE, 2010, pp. 1085–1088.
[84] R. Piersanti, P.C. Africa, M. Fedele, C. Vergara, L. Dedè, A.F. Corno, A. Quarteroni, Modeling cardiac muscle fibers in ventricular and atrial electrophysiology simulations, Comput. Methods Appl. Mech. Engrg. 373 (2021) 113468.
[85] H. Omrani, P. Drobinski, T. Dubos, Spectral nudging in regional climate modelling: how strongly should we nudge? Q. J. R. Meteorol. Soc. 138 (668) (2012) 1808–1813.
[86] J.R. Taylor, W. Thompson, An Introduction to Error Analysis: The Study of Uncertainties in Physical Measurements, vol. 2, Springer, 1982.
[87] A.H. Aletras, S. Ding, R.S. Balaban, H. Wen, DENSE: displacement encoding with stimulated echoes in cardiac functional MRI, J. Magn. Reson. (San Diego, Calif.: 1997) 137 (1) (1999) 247.
[88] J.H. Bracamonte, J.S. Wilson, J.S. Soares, Quantification of the heterogeneous effect of static and dynamic perivascular structures on patient-specific local aortic wall mechanics using inverse finite element modeling and DENSE MRI, J. Biomech. 138 (2022) 111119.
[89] M. Sermesant, H. Delingette, H. Cochet, P. Jais, N. Ayache, Applications of artificial intelligence in cardiovascular imaging, Nat. Rev. Cardiol. 18 (8) (2021) 600–609.
[90] K. Siegersma, T. Leiner, D. Chew, Y. Appelman, L. Hofstra, J. Verjans, Artificial intelligence in cardiovascular imaging: state of the art and implications for the imaging cardiologist, Neth. Hear. J. 27 (2019) 403–413.
[91] Q. Meng, W. Bai, D.P. O'Regan, D. Rueckert, DeepMesh: Mesh-based cardiac motion tracking using deep learning, IEEE Trans. Med. Imaging (2023).
[92] M.M. Bissell, F. Raimondi, L. Ait Ali, B.D. Allen, A.J. Barker, A. Bolger, N. Burris, C.J. Carhäll, J.D. Collins, T. Ebbers, et al., 4D flow cardiovascular magnetic resonance consensus statement: 2023 update, J. Cardiovasc. Magn. Reson. 25 (1) (2023) 1–24.
[93] J. Busch, D. Giese, L. Wissmann, S. Kozerke, Reconstruction of divergence-free velocity fields from cine 3D phase-contrast flow measurements, Magn. Reson. Med. 69 (1) (2013) 200–210.
[94] R. Chabiniok, V.Y. Wang, M. Hadjicharalambous, L. Asner, J. Lee, M. Sermesant, E. Kuhl, A.A. Young, P. Moireau, M.P. Nash, et al., Multiphysics and multiscale modelling, data–model fusion and integration of organ physiology in the clinic: ventricular cardiac mechanics, Interface Focus. 6 (2) (2016) 20150083.
[95] P.C. Di Leoni, A. Mazzino, L. Biferale, Inferring flow parameters and turbulent configuration with physics-informed data assimilation and spectral nudging, Phys. Rev. Fluids 3 (10) (2018) 104604.
[96] M. Bustamante, F. Viola, J. Engvall, C.J. Carlhäll, T. Ebbers, Automatic time-resolved cardiovascular segmentation of 4D flow MRI using deep learning, J. Magn. Reson. Imaging 57 (1) (2023) 191–203.
[97] H. Berhane, M. Scott, M. Elbaz, K. Jarvis, P. McCarthy, J. Carr, C. Malaisrie, R. Avery, A.J. Barker, J.D. Robinson, et al., Fully automated 3D aortic segmentation of 4D flow MRI for hemodynamic analysis using deep learning, Magn. Reson. Med. 84 (4) (2020) 2204–2218.